Distributed Continuous Time-Varying Optimization for Microgrids with Heterogeneous Renewable Energy Systems

Runfan Zhang, *Member, IEEE,* Zixuan Liu, Tong He, Branislav Hredzak, *Senior Member, IEEE*, Thomas Morstyn, *Senior Member, IEEE*, Zhaohong Bie, *Fellow, IEEE*

***Abstract*—Microgrid control systems are implemented using a hierarchical framework comprising primary, secondary and tertiary control levels. This paper proposes a distributed, time-varying optimization method for the secondary control level of heterogeneous energy sources (photovoltaics and batteries) in a microgrid. The method addresses time-varying objectives and constraints while achieving frequency and voltage regulation and optimal power sharing. Its main advantages are: (i) provision of continuous-time optimal control inputs that adapt to fast changes in generation and load; (ii) seamless interaction with grid forming and grid following converters; (iii) adaptive real/reactive power sharing and battery state-of-charge balancing based on net power and state of charge; and (iv) implementation over a sparse neighbor-to-neighbor communication graph. Real-time validation on a modified IEEE 13- and 37- test feeder using RTDS with a server-side solver, hardware-in-the-loop, confirms feasibility. Compared with established distributed secondary control schemes, the proposed controller reduces frequency and voltage root-mean-square regulation errors, lowers the maximum observed voltage deviation under load or renewable disturbances, and achieves a lower cumulative operating cost while maintaining all battery state-of-charge trajectories balanced. Scalability and heterogeneity are further demonstrated on an islanded IEEE 37-bus case with mixed grid forming and grid following resources.**

***Index Terms*—Distributed time varying optimization, microgrids, photovoltaic, battery energy storage, secondary control, grid following control, grid forming control, heterogeneous energy sources, hardware-in-loop**

NOMENCLATURE

$v_{odi},\ v_{oqi},$ q_i	Output voltages decoupled along the d-axis and q-axis and reactive power of the i-th voltage source converter (VSC).
ω_i, p_i	Frequency and output active power of the i-th VSC .
$v_{odi}^{ref}, \omega_i^{ref}$	Voltage and frequency references to be designed by the secondary control.
n_i, m_i	Voltage droop coefficient and frequency droop coefficient.
$\mathcal{G}_{fm}, \mathcal{G}_{fl}$	Set of converters in the grid forming mode and the grid following mode, respectively.
p_i^{ref}, q_i^{ref}	Real power and reactive power set-points to be designed by the secondary control.
ω_{nrm}, v_{nrm}	Nominal frequency and voltage of a microgrid (μG).
$\sigma\%$	Ratio of real power set-point to maximum power point tracking (MPPT) output power for the photovoltaics (PV) system.
$p_{\text{MPPT}i}$	MPPT output power of the i-th PV system.
$u_{\omega fmi},\ u_{vfmi},$ $u_{pfmi},\ u_{qfmi}$	Inputs of the proposed distributed time varying optimization control for frequency and voltage restorations, and the real and reactive power sharing for the i-th converter in the grid forming mode.
$u_{\omega fli},\ u_{vfli},$ $u_{pfli},\ u_{qfli}$	Inputs of the proposed distributed time varying optimization control for frequency and voltage restorations, and the real and reactive power sharing for the $i-$th converter in the grid following mode.
N	Number of converter agents in a μG.
$\mathcal{L}, [\mathcal{L}]_{ij}$	Laplace matrix of the sparse communication topology and $[\mathcal{L}]_{ij}$ is the element of $\mathcal{L}$.
ε	Set of all communication links between agents.
$f_{\omega i}$	Objective function for frequency control.
$\omega_{set}\,(t)$	Tracking objective of frequency, which could be a static value for an islanded μG or a time varying target from the tertiary level control system.
$\Delta\omega$	Allowable frequency deviation.
$\boldsymbol{\omega}$	Column vector form of ω_i.
$\mathbf{0}$	A $N_{fm} \times 1$ column vector with all elements of 0.
ω^*	Optimal solution of the converter agent frequency optimal control problem with local constraints and sparse constraints.
$\mathbf{1}$	Right eigenvector associated with $\lambda_1 = 0$ of $\mathcal{L}$, which is a balanced matrix.
$< \omega >$	A positive scalar denoting the same frequency value for each converter agent, which is $\omega_i = \omega_j = \cdots =< \omega >, i,\ j \in \mathcal{G}_{fm}$.
$\phi_{\omega i}$	Modified objective function with logarith-

Runfan Zhang, Zixuan Liu, Tong He, and Zhaohong Bie are with the School of Electrical Engineering, Xi'an Jiaotong University, Xi'an 710049, Shaanxi, China (Email: r.zhang@xjtu.edu.cn). Branislav Hredzak is with the School of Electrical Engineering and Telecommunications, UNSW Sydney, Sydney, NSW 2052, Australia (Email: b.hredzak@unsw.edu.au). Thomas Morstyn is with the Department of Engineering Science, University of Oxford, U.K. (Email: thomas.morstyn@eng.ox.ac.uk).

This work was supported by the National Natural Science Foundation of China (No. 52207135).

	mic type indicator function for frequency optimal control.
$\rho_{\omega i}(t)$	Barrier parameter for the indicator function for frequency optimal control.
$\sigma_{\omega i}(t)$	Slack function for frequency control, enlarging the initial feasible set.
$a_{\omega i},\ b_{\omega i},$ $c_{\omega i},\ d_{\omega i}$	Parameters of the logarithmic type indicator function for frequency optimal control.
$\mathfrak{L}_{\omega}$	Lagrangian of the modified frequency optimal problem.
λ_{ω}	Lagrange multiplier for frequency optimal control.
$(\omega^*,\ \lambda_{\omega}^*)$	Optimal primal-dual pair for (18).
u_{ω}	Optimal time varying controller incorporating the Newton-like correction term.
$\mathfrak{P}\nabla_{\omega}\sum_{i}\phi_{\omega i}$	Newton-like correction term for frequency optimal control.
$\mathfrak{P}, \bar{\varepsilon}$	Parameters of Newton-like correction term.
φ_{ω}	An auxiliary vector, which represents the dynamics of $\mathcal{L}\dot{\lambda}_{\omega}$.
$\mathrm{sign}(\chi), \kappa$	Signum function and parameter of φ_{ω}.
β	Fixed control gain of the secondary time varying optimization frequency control.
τ	Step size of control discretization.
f_{vodi}	Objective function for voltage control.
$v_{vodset}(t)$	Nominal voltage of μG, which is determined by the higher level optimization control system.
Δv	Allowable voltage deviation of the μG voltage.
ϕ_{vi}	Modified objective function with logarithmic type indicator function for voltage control.
ρ_{vi}	Barrier parameter for the indicator function for voltage optimal control.
$\sigma_{vi}(t)$	Slack function of ϕ_{vi}.
$a_{vi},\ b_{vi},$ $c_{vi},\ d_{vi}$	Barrier parameter of the logarithmic type indicator function for voltage optimal control.
$\mathfrak{L}_{v}$	Lagrangian of the modified voltage optimal problem.
u_{vodi}	Local time varying optimization voltage control.
$\bar{v}_i$	Average voltage estimation of the $i-$th converter agent.
γ	Tune-able parameter with $\gamma > 0$ for distributed average voltage estimation.
$\phi_{\bar{v}_i}$	Modified objective function with Logarithmic type indicator function for average voltage optimization problem.
$\mathfrak{L}_{\bar{v}}$	Lagrangian of the average voltage optimization.
λ_{ω}	Lagrange multiplier for the sparse average voltage constraints.
u_{vodi}	Distributed time varying optimization average voltage control.
p_{pvi}, p_{besi}	Output power for PV and battery energy system (BES), respectively.
$f_{\mathcal{Z}i}$	The objective function for real and reactive power.
c_1, c_2	Gains associated with the multi-objective function $f_{\mathcal{Z}i}$, which represent the costs of real power supply from the battery and reactive power injection, respectively.
$\tilde{p}_i$	Variable output power for BES under the distributed time varying power optimal control.
ϑ_i	Dynamic tuning gain to control the output power of BES.
p_{net}	μG net power.
ς_i	State of charge (SOC) of the $i-$th BES.
E_i	Size of the $i-$th BES in Ws.
$\tilde{\vartheta}_i$	Normalized form of ϑ_i.
$\bar{\vartheta}, \underline{\vartheta}$	Upper and lower boundaries of all ϑ_i.
$\alpha_{\vartheta}, \beta_{\vartheta}$	Parameters for the normalization of ϑ_i.
$\tilde{p}$	Column vector form of variable output power.
$\tilde{q}_i$	Variable reactive power for VSC reactive power optimal control.
$\tilde{q}$	Column vector form of variable reactive power.
p_{chri}, p_{dchri}	Maximum charging and discharging powers of BES.
$q_{\max i}$	Maximum limit of the reactive power.
s_{rtdi}	Rated apparent power of the $i-$th converter.
$\bar{\varsigma}, \underline{\varsigma}$	Upper and lower boundaries of all ς_i.
$\mathbf{g}_i(p_{besi},\ q_i)$	Compact form of constraints (43) to (45).
$\mathcal{Z}_i$	State variable composed of $\tilde{p}_i$ and $\tilde{q}_i$.
$\phi_{\mathcal{Z}i}$	Modified objective function with logarithmic type indicator function for real and reactive power optimization.
$\rho_{\mathcal{Z}i}$	Barrier parameter for the indicator function of power sharing optimization control.
$\sigma_{\mathcal{Z}i}(t)$	Slack function for real and reactive power optimization control.
$a_{\mathcal{Z}i},\ b_{\mathcal{Z}i},$ $c_{\mathcal{Z}i},\ d_{\mathcal{Z}i}$	Parameters of the logarithmic type indicator function for real and reactive power optimization.
$\mathfrak{L}_{\mathcal{Z}}$	Lagrangian of the real and reactive power optimization.
$\lambda_{\mathcal{Z}}$	Lagrange multiplier for the sparse real and reactive power sharing constraints.
$u_{\mathcal{Z}i}$	$u_{\mathcal{Z}i} = [u_{pi},\ u_{qi}]^{\mathrm{T}}$, the distributed secondary time varying optimization control for real and reactive power regulation.
f_{pvi}	Objective function for real power optimization.
$p_{\mathrm{MPPT}i}$	MPPT output power.
c_{pv1}, c_{pv2}	Gains for the multi-objectives of the PV system alone.
$\widehat{p}_i$	Ratio of PV output power to MPPT output

power.

$\widehat{\mathbf{p}}$ Column vector form of $\widehat{p}_i$.

I. Introduction

MICROGRIDS (μGs) are power systems operating at a small scale within localized regions. The μGs employ a comprehensive hierarchical control framework with different control levels [1], each designed to address specific operational challenges [2]. They can interface with heterogeneous energy sources which can be categorized into active and passive sources [3]. Active sources have controllable output powers and can regulate μGs voltage and frequency. Battery energy storage systems (BESs) and small generators powered by diesel or natural gas serve as active sources. They enhance the stability and reliability of μGs by delivering controllable output power. Additionally, some units provide voltage and frequency references for μGs. In contrast, passive sources are not directly controllable and inject stochastically varying power into μGs. Photovoltaics (PV) and small wind turbines, which are conventionally not actively controlled, contribute variable power in μGs [4]. Despite this, they can still assist in voltage and frequency regulation through specifically designed control systems.

With a holistic control framework, μGs can operate in both islanded and grid connected modes [5]. μGs may intentionally or involuntarily disconnect from the main grid to reduce losses on long feeders, isolate faults and associated voltage excursions, or ride through upstream outages [6]. Once islanded, limited local energy reserves and the fast, stochastic variability of renewable generation make frequency, voltage, and power balance control more difficult.

A rigorously coordinated control architecture is therefore required to sustain stable and efficient islanded operation. A hierarchical structure with primary, secondary, and tertiary levels is widely adopted [7]. At the primary level, grid forming (GFM) units (e.g., battery energy storage) establish local voltage and frequency through droop control, while grid following (GFL) units (e.g., PV converters) synchronize via phase-locked loops and inject their available real and reactive power [8]. This separation of roles provides the foundation upon which higher levels can restore nominal setpoints, optimize power sharing, and enforce operational constraints. Converters controlled by the grid forming method provide the frequency and voltage references, while grid following converters track frequency via a phase-locked loop (PLL). Typically, converters using the grid following control method do not need to support μGs frequency and voltage. However, in islanded μGs, where reliable energy sources for forming frequency and voltage are limited, grid following controlled converters must regulate their output power in response to frequency and voltage deviations to alleviate the burden on grid forming controlled converters [9]. It is necessary to coordinate the grid following and forming control at the higher control level. Thus, the cooperation between active and passive energy sources distributed in μGs with different primary control principles presents another significant challenge for the secondary control of μG [10].

Secondary control in μGs encounters persistent challenges: (i) restoring frequency and voltage while preserving accurate active and reactive power sharing; (ii) coping with rapid, stochastic PV output; (iii) maintaining stability under unbalanced and time-varying loads and energy sources output powers; (iv) coordinating heterogeneous grid-forming and grid-following converters with differing internal dynamics; (v) scaling to larger fleets without excessive communication or model burden; and (vi) reconciling trade-offs among voltage regulation, reactive power sharing, economic operation, and dynamic performance. Existing methods address these points only in part. A fast, robust, and adaptive secondary control framework that natively handles heterogeneity and multi-objective trade-offs remains an open need.

Existing secondary coordination strategies for GFM and GFL converters cover islanded and grid-connected or weak-grid conditions [11], [12]. Representative approaches include: unified modeling with consensus layers and extended state observers to handle disparate inner dynamics [13]; voltage–current duality based unified models enabling μ-synthesis robust control for disturbance and harmonic rejection [14]; and leader–follower schemes where GFM units set system voltage and frequency while GFL units adjust power for sharing objectives [10]. While effective in defined scenarios, many rely on fixed operating points, detailed unified models that are costly to scale, or limited mechanisms to accommodate rapidly time-varying objectives and constraints. This motivates secondary control formulations that natively handle heterogeneity, multi-objective trade-offs, and fast operating condition variations.

Beside the equal/proportional power sharing control, μG optimization typically aims to achieve objectives such as economical dispatch among distributed generators and technical performance improvements, including power loss reduction [15]. Additionally, optimal operation for BES has been reported to save on power loss and degradation costs. These optimization methods update models and solutions on a minute-scale. The foregoing μG optimization methods are batch based: at each time step a static problem is solved, or forced to converge, before the next update. This need to finish a full solve within the interval limits responsiveness to rapid, high-frequency variations in renewable energy source generation and load, where control decisions must adapt on shorter sub-interval timescales. While, the output power from renewable energy sources varies over time, causing the objectives and their local and global constraints to become time-varying [16]. Thus, μGs optimization problems, particularly those aimed at improving power quality, naturally and suitably adopt time-varying optimization.

Extensive work has examined time-varying optimization. Methods are commonly grouped by their temporal model: continuous-time and discrete-time. In continuous-time formulations, the optimizer is expressed as an ordinary differential equation that tracks the moving minimizer [17]. When discretization with sufficiently small steps, these dynamics closely approximate the underlying system and admit Lyapunov-based stability guarantees; sliding-mode variants can additionally ensure finite-time convergence [18].

In contrast, discrete-time methods operate on a fixed sampling sequence and typically implement a prediction–correction structure [19]. Distributed prediction–correction Newton schemes forecast the evolution of the objective and constraints and then refine the iterate, improving tracking of fast changes. Predefined-time approaches enforce convergence within a fixed horizon independent of the initial state [20]. Primal–dual mirror descent variants achieve sublinear dynamic and static regret, gap to the moving optimum, while keeping constraint violations bounded [21]. These methods return approximate trajectories whose tracking error is determined by sampling period, model mismatch, and prediction accuracy, and they naturally support asynchronous or event-triggered updates, lowering communication burden.

An alternative view classifies time-varying optimization methods by exploiting predicted system evolution. Time-structured, prediction-based, methods require a model or prediction of future states to pre-empty variations and accelerate tracking. Prediction–correction and fixed-time schemes have achieved sub-second economic dispatch and voltage regulation in μG studies [22]. Under standard strong convexity and smoothness conditions, bounded tracking error or asymptotic optimality have been achieved. In contrast, time-unstructured methods, only depend on the latest sample or system states, ignore future evolution [23]. They are simpler and communication-efficient but typically exhibit larger instantaneous tracking errors, although cumulative, dynamic/static, regret can still be kept sublinear over long horizons [24].

Time-varying optimization provides a mathematically rigorous framework for real-time decision-making in dynamic systems, which potentially adapts μG distributed renewable energy sources with rapid variations on its output powers. The time-varying optimization method has been used in power systems to handle stochastic loads and renewable energy output fluctuations for frequency response [25], power dispatching [26], and optimal power flow [27], [28]. Time-varying delivery intervals derived from predicted frequency nadir enable optimization of fast frequency response, as nadir timing strongly shapes scheduling decisions [25]. Prediction–correction time-varying dispatch methods accommodate rapidly fluctuating distribution injections and achieve asymptotically vanishing tracking error [26]. Moreover, prediction-based primal–dual interior-point schemes enhance tracking accuracy for time-varying AC optimal power flow [28]. Distributed energy sources can support voltage regulation at the secondary level using the time-varying optimization method with the linear approximation of AC power flow and Lagrangian regularization method [29].

Furthermore, considering the distributed nature of energy sources in μGs, distributed time-varying optimization can effectively manage large-scale energy sources for multiple purposes [30]. The distributed method allows the centralized global problem to be decoupled into multiple sub-problems, which can be solved in parallel [31]. These sub-problems communicate with each other via a neighbor-to-neighbor sparse communication network. Both distributed continuous time-varying optimization methods [32] and discrete time-varying optimization methods [33] can solve optimal problems with varied objectives and equality or inequality constraints [34].

Distributed continuous-time methods combine graph-based consensus with sliding-mode or Hessian, a second-order, correction to drive all agents toward a common optimum while satisfying nonlinear local inequality constraints [32]. Complementary discrete-time schemes allow asynchronous computation, measurement, and communication while still track the moving optimum with guaranteed convergence and bounded error [33]. Prediction-based formulations have enabled online multi-period power flow optimization by forecasting system states and decoupling sensitivities [27]. Despite these advances, only a few studies have deployed such time-varying distributed optimizers in μGs with heterogeneous, GFM and GFL, resources [35].

Motivated by the above discussion, this paper proposes a time-structured secondary level distributed time-varying optimization control framework for μGs with different types of energy sources. These energy sources can be PVs, BESs, or a combination of both. Typically, BESs are controlled by the grid forming mode at the primary level, while other sources are controlled by the grid following mode.

The primary contributions of this paper are:

1) A feedback-linearization–based secondary control framework for heterogeneous energy resources operating in both GFL and GFM modes.
2) A distributed, time-structured, continuous-time time-varying optimization scheme that simultaneously addresses diverse and time-varying control objectives across heterogeneous resources.

The salient features of the proposed distributed time-varying optimization framework are:

1) It can track dynamic objectives under continuous time-varying constraints via a time structured algorithm. Therefore, the proposed optimization method maintains frequency, voltage or average voltage, and power sharing during variations in renewable energy sources or loads distributed in the μG.
2) It can interact with energy sources using both grid forming and grid following primary control modes. This enables effective cooperation among heterogeneous energy sources.
3) It requires only a neighbor-to-neighbor communication network, leveraging the advantages of a sparse communication network-based control system.

II. Principles and Framework of μG Control

In this paper, a hierarchical control framework is adopted to coordinate heterogeneous μG resources. Fig. 1 outlines the structure. At the primary level, converters operate either in GFM or GFL mode with droop-based control. GFL units, typically storage, set local voltage and frequency references. GFM units, PV interfaced converters, synchronize to these references and regulate power injection.

To unify the behavior of devices with different primary control modes, a secondary layer is proposed using feedback linearization. This layer supplies dynamic reference signals for

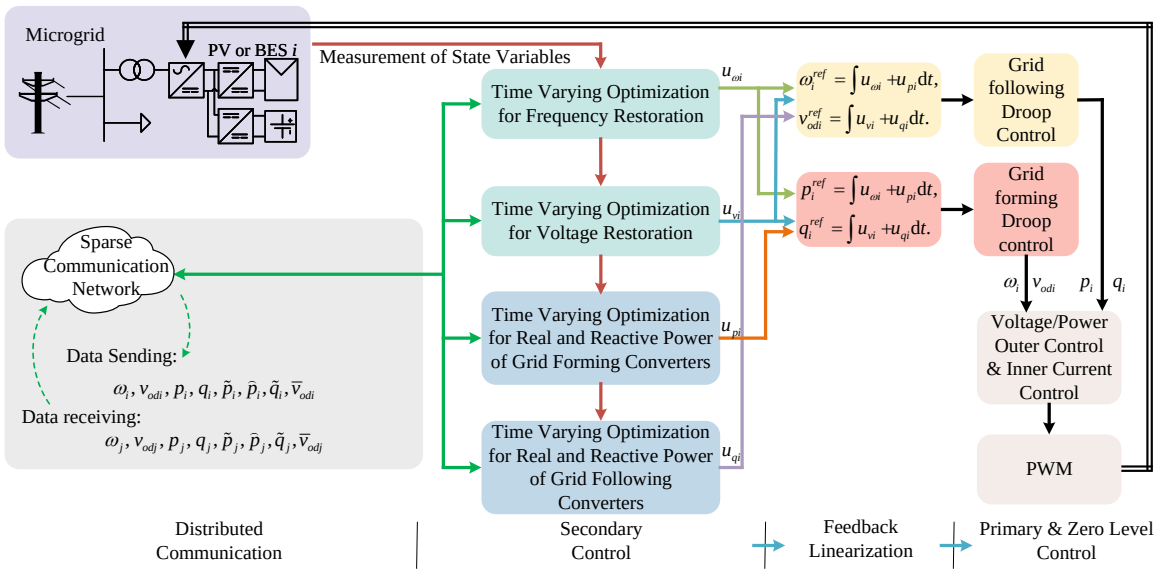

Fig. 1: Block diagram of the proposed distributed secondary control and its interactions with the primary control system. The secondary control signals are transmitted to the feedback linearization blocks, which then generate the primary control signals.

frequency, voltage or average voltage, and real/reactive power sharing. It establishes the closed-loop state–input relationships required for the distributed continuous time-varying optimization algorithms developed in the subsequent sections.

A. Primary Control for Heterogeneous Energy Sources

In heterogeneous μGs, converter-interfaced resources operate either in GFM or GFL mode, decided by the capability and control objective. GFM units, typically battery energy storage or other dispatchable sources, apply droop control to establish system frequency and local voltage magnitude [36]. GFL units, such as PV inverters, treat the network as a voltage reference; a PLL estimates frequency and phase, and outer power controllers regulate active and reactive injections based on available generation and higher-level setpoints [37].

1) Droop Control for Grid Forming Mode: Normally, frequency and voltage droop control is implemented in the grid forming mode. Specifically, the $f-p$ and $v-q$ droop equations determine the phase angle and voltage references for local PI based outer and inner control loops.

$$\omega_i = \omega_i^{ref} - m_i p_i,\ i \in \mathcal{G}_{fm}, \tag{1}$$

$$v_{odi} = v_{odi}^{ref} - n_i q_i,\ v_{oqi} = 0,\ i \in \mathcal{G}_{fm}, \tag{2}$$

where, v_{odi}, v_{oqi} and q_i represent the i-th voltage source converter (VSC) output voltages decoupled along the d-axis and q-axis, operating on the converter local synchronous reference frame, and reactive power, respectively; ω_i and p_i indicate the frequency and the i-th VSC output active power, while v_{odi}^{ref} and ω_i^{ref} are the nominal voltage and frequency values. These nominal values are set by the secondary level control via a neighbor-to-neighbor communication protocol discussed in subsequent sections; n_i and m_i denote the corresponding droop coefficients.

With the frequency and voltage references established, local control tracks the output voltages v_{odi} and v_{oqi} through an inner current loop and an outer voltage loop. The overall configuration of the primary and local controls for grid forming mode is presented in Fig. 2a. In a μG, at least one converter must operate in grid forming mode to establish frequency and voltage. Therefore, distributed energy storage systems are an essential requirement for operating in grid forming mode.

2) Droop Control for Grid Following Mode: In the grid following mode, the frequency and phase angle are measured locally via a PLL. Then, the $p-f$ and $q-v$ droop equations are implemented to generate the real and reactive power references as

$$p_i = p_i^{ref} - m_i^{-1}\left(\omega_i - \omega_{nrm}\right),\ i \in \mathcal{G}_{fl}, \tag{3}$$

$$q_i = q_i^{ref} - n_i^{-1}\left(v_{odi} - v_{nrm}\right),\ i \in \mathcal{G}_{fl}, \tag{4}$$

where p_i^{ref} and q_i^{ref} are the real power and reactive power set-points; ω_{nrm} and v_{nrm} are the nominal frequency and voltage of μG. The converter operating in grid following control mode is able to provide real and reactive power by varying its output frequency and voltage, respectively. It should be noted that, if the convert has only a PV system without BESS support, the real power set-point should be reduced slightly from that of the maximum power point tracking (MPPT) power for the purposes of superior frequency regulation, such that $p_i^{ref} = \sigma\% p_{\text{MPPT}i}$, where $\sigma\% \leq 1$, and $p_{\text{MPPT}i}$ is the MPPT output power of the PV system. In this case, $p-f$ droop control can be rewritten as,

$$p_i = \sigma\% p_{\text{MPPT}i} - m_i^{-1}\left(\omega_i - \omega_{nrm}\right)\ i \in \mathcal{G}_{fl}. \tag{5}$$

Then, based on the power references, the outer power control sets the inductor current set-points in the $d-q$ axis, respectively. The overall control structure of the primary droop control, outer power control, and inner current control is shown in Fig. 2b.

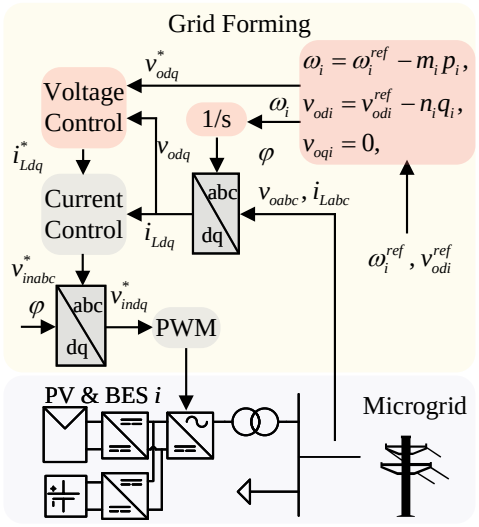

(a) Grid forming control

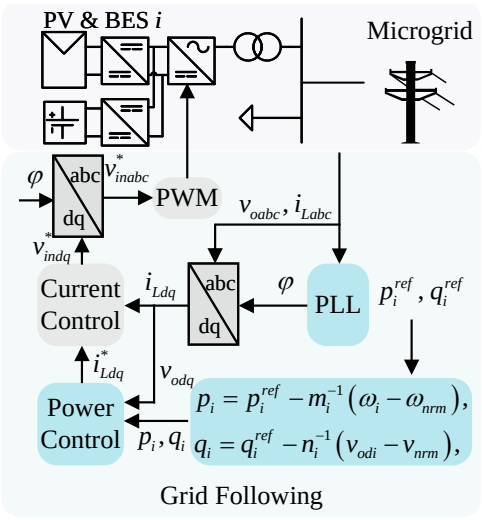

(b) Grid following control

Fig. 2: Block diagram of the primary droop control: (a) grid forming control; (b) grid following control.

B. Secondary Control Framework for Heterogeneous Energy Sources

Secondary control coordinates grid forming and grid following converters to restore frequency and voltage and enforce power sharing under variable renewable energy source generation and load. A feedback linearization layer [38] maps each regulated state, frequency, voltage or average voltage, real and reactive power terms, to virtual inputs. Continuous time-varying optimization then computes these inputs in real time from changing objectives and constraints, e.g., renewable fluctuations, voltage and frequency limits, and output power boundaries. The linearization layer translates the optimized virtual inputs into primary droop or power references for each converter, providing a unified interface that enables heterogeneous devices to cooperate using only neighbor-to-neighbor communication. For converters operating in grid forming modes given by (1) and (2), set

$$\begin{aligned} &\dot{\omega}_i = u_{\omega fmi},\ m_i\dot{p}_i = u_{pfmi}, \\ &\dot{v}_{odi} = u_{vfmi},\ n_i\dot{q}_i = u_{qfmi}, i \in \mathcal{G}_{fm}, \end{aligned} \tag{6}$$

where $u_{\omega fmi}$, u_{vfmi}, u_{pfmi} and u_{qfmi} are the control inputs of frequency and voltage restorations, and the real and reactive power sharing for the i-th converter in the grid forming mode; $\mathcal{G}_{fm}$ denotes the set of converters in the grid forming mode.

Then, the substitution of $u_{\omega i}$, u_{vi}, u_{pi} and u_{qi} into (1) and (2) gives the voltage and frequency references for the lower control loops as,

$$\begin{aligned} \omega_i^{ref} &= \int (u_{\omega fmi}+u_{pfmi})\,\mathrm{d}t, \\ v_{odi}^{ref} &= \int (u_{vfmi}+u_{qfmi})\,\mathrm{d}t, i \in \mathcal{G}_{fm}. \end{aligned} \tag{7}$$

Applying the feedback linearization, the states of each converter agent in the grid following mode can be described as,

$$\begin{aligned} &m_i^{-1}\dot{\omega}_i = u_{\omega fli},\ \dot{p}_i = u_{pfli}, \\ &n_i^{-1}\dot{v}_{odi} = u_{vfli},\ \dot{q}_i = u_{qfli}, i \in \mathcal{G}_{fl}, \end{aligned} \tag{8}$$

$$\begin{aligned} p_i^{ref} &= \int (u_{\omega fli}+u_{pfli})\,\mathrm{d}t, \\ q_i^{ref} &= \int (u_{vfli}+u_{qfli})\,\mathrm{d}t, i \in \mathcal{G}_{fl}, \end{aligned} \tag{9}$$

where $\mathcal{G}_{fl}$ denotes the set of the converters under grid following mode. The proposed time varying optimization will determine the control inputs $u_{\omega fli}$, u_{vfli}, u_{pfli} and u_{qfli} based on the varied objectives and constraints. Then, the frequency, voltage, real and reactive power references for the primary droop controls can be obtained via (7) and (9) respectively.

III. Distributed Time Varying Optimization with Sparse Coupled Constraints

A. Sparse Communication Network

In the proposed distributed method, a converter with its control system is treated as an agent. A converter agent shares its local information with its neighbor via a sparse communication network. Suppose there are N converter agents in a μG. The sparse communication topology can be described by the following Laplace matrix $\mathcal{L} \in \Re^{N\times N}$,

$$[\mathcal{L}]_{ij} = \begin{cases} 1, & \{i,j\} \in \varepsilon,\ j \neq i, \\ 0, & \{i,j\} \notin \varepsilon,\ j \neq i, \\ -\sum\limits_{k=1,k\neq i}^{N} [\mathcal{L}]_{ik}, & j = i, \end{cases} \tag{10}$$

where $[\mathcal{L}]_{ij}$ is the element of $\mathcal{L}$; ε is the set of all communication links between agents. In this paper, bidirectional communication channels are assumed. Thus, there is $[\mathcal{L}]_{ij} = [\mathcal{L}]_{ji}$, $i \neq j$.

B. Distributed Time Varying Optimization for Photovoltaic and Battery Energy Storage Systems

Normally, PV systems with BESs are controlled in the GFM mode. The objectives of the proposed continuous time-varying optimization control for PVs and BESs include establishing μG frequency and voltage set-points. These set-points may be time-varying or static, depending on the tertiary level control system or islanded operation of μGs. Additionally, the optimization aims to achieve optimal operation of BESs considering cost and reactive power support. Therefore, the time-varying optimization problem can be formulated as follows:

1) Frequency Optimization: Decision variables are selected as ω_i, v_{odi}, p_i and q_i respectively. For the frequency tracking, the optimal problem is

$$\min_{\omega_i} f_{\omega i}(\omega_i) = \|\omega_i - \omega_{set}(t)\|_2^2, i \in \mathcal{G}_{fm}, \tag{11}$$

where $\omega_{set}(t)$ is the tracking objective, which could be a static value for an islanded μG or a time varying target from the tertiary level control system. The frequency should be bounded by

$$\omega_{set}(t) - \Delta\omega \le \omega_i \le \omega_{set}(t) + \Delta\omega, i \in \mathcal{G}_{fm}, \tag{12}$$

where $\Delta\omega$ is the allowable frequency deviation. Another constraint for the frequency regulation is that there is only one frequency value in the μG,

$$\omega_i = \omega_j = \cdots, i,\ j \in \mathcal{G}_{fm}. \tag{13}$$

The frequency constraint can be rewritten considering the sparse communication network $\mathcal{L}$ as,

$$\mathcal{L}\omega = \mathbf{0}, \tag{14}$$

where $\omega = \left[\ \omega_1,\ \cdots,\ \omega_i,\ \cdots,\ \omega_{Nfm}\ \right]^T, i \in \mathcal{G}_{fm}$, $\mathbf{0}$ is a $N_{fm} \times 1$ column vector with all elements 0.

Then, the frequency time varying optimization can be summarized as,

$$\begin{aligned} \omega^*(t) = \arg\min & \sum_i f_{\omega i}(\omega_i(t), t) \\ \text{s.t. } & (12) \text{ and } (14), \\ & i \in \mathcal{G}_{fm}, \end{aligned} \tag{15}$$

where ω^* is the optimal solution of the converter agent objective function, local constraints and sparse constraints. In the above optimization problem, frequency constraint (13) is rewritten as the compact form (14). In accordance with [39], $\mathbf{1}$ is the right eigenvector associated with $\lambda_1 = 0$ of $\mathcal{L}$, which is a balanced matrix. In addition with the constraint (12), there is $\omega \neq \mathbf{0}$. Thus, the unique solution of (14) is $\omega = <\omega> \mathbf{1}$, where $<\omega>$ is a positive scalar denoting the same frequency value for each converter agent, i.e. $<\omega> = \omega_i = \omega_j = \cdots, i,\ j \in \mathcal{G}_{fm}$.

The proposed distributed time varying optimal control algorithm aims to find the control u_{ω_i}, to maintain and converge the frequency to the optimal frequency solution $\omega^*(t)$ such that,

$$\lim_{t\to\infty} (\omega_i(t) - \omega^*(t)) = 0, i \in \mathcal{G}_{fm}. \tag{16}$$

First, to deal with the local constraints, a penalized term is introduced for the frequency optimization problem. In this paper, a logarithmic type indicator function is implemented as,

$$\begin{aligned} \phi_{\omega i} = & \|\omega_i - \omega_{set}(t)\|_2^2 \\ & -\frac{1}{\rho_{\omega i}(t)} \left[\ln\left(\sigma_{\omega i}(t) - (\omega_i - \omega_{set}(t) - \Delta\omega)\right)\right. \\ & \left. +\ln\left(\sigma_{\omega i}(t) - (-\omega_i + \omega_{set}(t) - \Delta\omega)\right)\right], i \in \mathcal{G}_{fm}, \end{aligned} \tag{17}$$

where $\rho_{\omega i}(t) > 0$ is a parameter for the indicator function, $\sigma_{\omega i}(t)$ is a slack function, enlarging the initial feasible set; where $\rho_{\omega i}(t) = a_{\omega i} e^{b_{\omega i} t}$, and $\sigma_{\omega i}(t) = c_{\omega i} e^{-d_{\omega i} t}$ with $a_{\omega i} > 0,\ b_{\omega i} > 0,\ c_{\omega i} > 0$, and $d_{\omega i} > 0$.

Then, the Lagrangian of the modified frequency optimal problem with barrier (17) and sparse constraints (14) can be written in a compact form as,

$$\mathfrak{L}_\omega = \sum_i \phi_{\omega i} + \lambda_\omega^{\mathrm{T}} \mathcal{L}\omega, i \in \mathcal{G}_{fm}, \tag{18}$$

where λ_ω is the Lagrange multiplier. Because the quadratic tracking term in (17) and the penalized logarithmic barrier (with $\sigma_{\omega i}(t) > 0,\ \rho_{\omega i}(t) > 0$) are convex, and the bound constraints in (12) are convex, $\phi_{\omega i}$ is convex and twice continuously differentiable. The modified unconstrained time varying optimal problem is strongly convex in ω and concave in λ_ω. Invoked by the primal-dual method, the optimal primal-dual pair $(\omega^*,\ \lambda_\omega^*)$ for (18) is unique at $t \ge 0$, which must satisfy the KKT conditions:

$$\begin{aligned} \nabla_\omega \mathfrak{L}_\omega &= \nabla_\omega \sum_i \phi_{\omega i}|_{\omega=\omega^*} + \mathcal{L}^{\mathrm{T}} \lambda_\omega^* = \mathbf{0}, \\ \nabla_{\lambda_\omega} \mathfrak{L}_\omega &= \mathcal{L}\omega^* = \mathbf{0}, i \in \mathcal{G}_{fm}. \end{aligned} \tag{19}$$

The derivative of both sides of (19) is also $\mathbf{0}$:

$$\begin{aligned} & \begin{bmatrix} \nabla_{\omega\omega} \sum_i \phi_{\omega i} & \mathcal{L} \\ \mathcal{L}^{\mathrm{T}} & \mathbf{0} \end{bmatrix} \begin{bmatrix} \dot{\omega}^* \\ \dot{\lambda}_\omega^* \end{bmatrix} + \begin{bmatrix} \nabla_{\omega\rho} \sum_i \phi_{\omega i} \dot{\rho}_\omega(t) \\ 0 \end{bmatrix} \\ & + \begin{bmatrix} \nabla_{\omega\sigma} \sum_i \phi_{\omega i} \dot{\sigma}_\omega(t) \\ 0 \end{bmatrix} + \begin{bmatrix} \nabla_{\omega t} \sum_i \phi_{\omega i} \\ 0 \end{bmatrix} = 0, i \in \mathcal{G}_{fm}. \end{aligned} \tag{20}$$

Then, the dynamic system of $\dot{\omega}^*$ can be solved from (20) as,

$$\begin{aligned} \dot{\omega}^* = -\left[\nabla_{\omega\omega} \sum_i \phi_{\omega i}\right]^{-1} & \left[\mathcal{L}\dot{\lambda}_\omega^* + \nabla_{\omega\rho} \sum_i \phi_{\omega i} \dot{\rho}_\omega(t)\right. \\ & \left. + \nabla_{\omega\sigma} \sum_i \phi_{\omega i} \dot{\sigma}_\omega(t) + \nabla_{\omega t} \sum_i \phi_{\omega i}\right], i \in \mathcal{G}_{fm}. \end{aligned} \tag{21}$$

The tracks of dynamic system (21) satisfies the KKT conditions (19). To design the optimal time varying controller, a Newton-like correction term is introduced [40]. Thus, the controller u_ω can be obtained by

$$\begin{aligned} \dot{\omega} = -\left[\nabla_{\omega\omega} \sum_i \phi_{\omega i}\right]^{-1} & \left[\mathfrak{P}\nabla_\omega \sum_i \phi_{\omega i} + \mathcal{L}\dot{\lambda}_\omega\right. \\ & \left. + \nabla_{\omega\rho} \sum_i \phi_{\omega i} \dot{\rho}_\omega(t) + \nabla_{\omega\sigma} \sum_i \phi_{\omega i} \dot{\sigma}_\omega(t) + \nabla_{\omega t} \sum_i \phi_{\omega i}\right], \\ & i \in \mathcal{G}_{fm}. \end{aligned} \tag{22}$$

where $\mathfrak{P}\nabla_\omega \sum_i \phi_{\omega i}$ is the Newton-like correction term, where $\mathfrak{P} = \bar{\varepsilon} I_N$, and $\bar{\varepsilon} > 0$. The term $\mathcal{L}\dot{\lambda}_\omega$ is designed for each converter agent as

$$\dot{\varphi}_{\omega i} = \mathrm{sign}(\omega_i - \omega_j)^\kappa,\ i, j \in \mathcal{G}_{fm}, \tag{23}$$

where φ_ω is an auxiliary vector, which represents the dynamics of $\mathcal{L}\dot{\lambda}_\omega$, $\varphi_\omega = \mathcal{L}\lambda_\omega$, $\varphi_\omega = \left[\ \varphi_{\omega 1}\ \cdots\ \varphi_{\omega i}\ \cdots\ \varphi_{\omega N}\ \right]^{\mathrm{T}}$, and $\lambda = \left[\ \lambda_1\ \cdots\ \lambda_i\ \cdots\ \lambda_N\ \right]^{\mathrm{T}}$; $\mathrm{sig}(\chi)^\kappa = \mathrm{sign}(\chi)|\chi|^\kappa$, for any $\chi \in \Re$, and $\kappa > 0$. $\mathrm{sign}(\chi)$ is the signum function as,

$$\mathrm{sign}(\chi) = \begin{cases} -1,\ \chi < 0, \\ 0,\ \chi = 0, \\ 1,\ \chi > 0. \end{cases} \tag{24}$$

Combining (22) and (23), the secondary time varying optimization frequency control with the fixed control gain $\beta > 0$ is

$$\dot{\omega}_i = u_{\omega i} = -\beta[\nabla_{\omega\omega}\phi_{\omega i}]^{-1}\left[\varepsilon\nabla_{\omega}\phi_{\omega i} + \mathrm{sig}(\omega_i - \omega_j)^{\kappa} + \nabla_{\omega\rho}\phi_{\omega i}\dot{\rho}_{\omega}(t) + \nabla_{\omega\sigma}\phi_{\omega i}\dot{\sigma}_{\omega i}(t) + \nabla_{\omega t}\phi_{\omega i}\right], i \in \mathcal{G}_{fm}. \tag{25}$$

Remark 1: The dynamic of the convergence of the proposed distributed time varying optimization control (22) can be tuned via the $\bar{\varepsilon}$. The larger $\bar{\varepsilon} > 0$ provides a faster convergence rate for the frequency control.

Remark 2: Practical implementation requires discretization (22) with step size $\tau > 0$. A standard ordinary differential equation discretization (e.g., forward Euler or higher order) yields a local truncation error of order $\mathcal{O}(\tau)$ (see [41]). After discretization, both $\bar{\varepsilon}$ and τ jointly affect stability and convergence; the effective step $\bar{\varepsilon}\tau$ must remain below a method-dependent bound to preserve the continuous-time properties [42]–[44]. Maintaining a bounded $\bar{\varepsilon}\tau$ enables consistent performance across hierarchical multi–time-resolution layers.

2) Voltage Optimization: The voltage optimization problem is analogous to the frequency optimization. However, unlike frequency, which requires a uniform value across all converter agents, voltage optimization requires sparse constraints due to the trade-off between reactive power sharing and voltage restoration [45]. In this paper, maintaining reactive power sharing involves two distinct methods to handle this trade-off: local voltage regulation or distributed average voltage consensus control.

a) Time Varying Optimization with Voltage Control: The primary objective of voltage control is to enhance power quality by eliminating voltage deviations. To achieve this, the voltage control must track the specified voltage references. Consequently, the objective function for voltage control is formulated to ensure adherence to these references as,

$$\min_{v_{odi}} f_{vodi}(v_{odi}(t)) = \|v_{odi}(t) - v_{vodset}(t)\|_2^2, i \in \mathcal{G}_{fm}. \tag{26}$$

where $v_{vodset}(t)$ is the nominal voltage of μG, which is determined by the higher level optimization control system. Also, the voltage is bounded by

$$v_{vodset}(t) - \Delta v \le v_{odi}(t) \le v_{vodset}(t) + \Delta v, i \in \mathcal{G}_{fm}. \tag{27}$$

where Δv is the allowable voltage deviation of the μG voltage. Then, to deal with the voltage boundaries, same as for the frequency control design method, a logarithmic type indicator function is introduced, and the objective function (26) is rewritten as

$$\phi_{vi} = \|v_{odi}(t) - v_{vodset}(t)\|_2^2 - \frac{1}{\rho_{vi}(t)}\left[\ln(\sigma_{vi}(t) - (v_{odi}(t) - v_{vodset}(t) - \Delta v)) + \ln(\sigma_{vi}(t) - (-v_{odi}(t) + v_{vodset}(t) - \Delta v))\right], i \in \mathcal{G}_{fm}, \tag{28}$$

where $\rho_{vi} > 0$ is the barrier function for the indicator function, $\sigma_{vi}(t)$ is a slack function. $\rho_{vi}(t) = a_{vi}e^{b_{vi}t}$, and $\rho_{vi}(t) = c_{vi}e^{-d_{vi}t}$ with $a_{vi} > 0$, $b_{vi} > 0$, $c_{vi} > 0$, and $d_{vi} > 0$. For the local voltage control mode, the Lagrangian is

$$\mathfrak{L}_v = \sum_i \phi_{vi}, i \in \mathcal{G}_{fm}. \tag{29}$$

Then, following the similar design procedure, the local time varying optimization voltage control is

$$\dot{v}_{odi} = u_{vodi} = -\beta[\nabla_{vivi}\phi_{vi}]^{-1}\left[\varepsilon\nabla_{vi}\phi_{vi} + \nabla_{vi\rho}\phi_{vi}\dot{\rho}_v(t) + \nabla_{vi\sigma i}\phi_{vi}\dot{\sigma}_{vi}(t) + \nabla_{vit}\phi_{vi}\right], i \in \mathcal{G}_{fm}. \tag{30}$$

b) Distributed Time Varying Optimization with Average Voltage Control: In this control mode, the average estimation voltage rather than the local measured voltage is implemented for the average voltage control. The average voltage estimation of converter agents can be obtained as [46],

$$\dot{\bar{v}}_i = \dot{v}_{odi} + \gamma\sum_{j\in\mathcal{N}_i}[\mathcal{L}]_{ij}(\bar{v}_j - \bar{v}_i), i \in \mathcal{G}_{fm}. \tag{31}$$

where $\bar{v}_i$ is the average voltage estimation of the i-th converter agent; γ is a tune-able parameter with $\gamma > 0$; $\bar{v}_i$ can observe the average voltage of all converter agents with any initial value $\bar{v}_i(0)$. Thus, there is $\lim_{t\to\infty}\left(\bar{v}_i(t) - \frac{1}{N}\sum_i v_{odi}(t)\right) = 0$. Then, substitution of v_{odi} by $\bar{v}_i$ in the voltage control objective (26), the local constraints (27) and the objective function (28) gives the average voltage optimization problem with the indicator function $\phi_{\bar{v}_i}$.

In the average voltage control mode, the sparse constraints ensure the average voltage restoration performance,

$$\mathcal{L}\bar{\mathbf{v}} = \mathbf{0}, \tag{32}$$

where $\bar{\mathbf{v}} = \left[\ \bar{v}_i, \ \cdots, \ \bar{v}_i, \ \cdots, \ \bar{v}_N\ \right]^T$. Then, the Lagrangian of the average voltage optimization with sparse constraints is,

$$\mathfrak{L}_{\bar{v}} = \sum_i \phi_{\bar{v}_i} + \lambda_v^{\mathrm{T}}\mathcal{L}\bar{\mathbf{v}}, i \in \mathcal{G}_{fm}. \tag{33}$$

where λ_ω is the Lagrange multiplier for the sparse average voltage constraints. Therefore, the distributed time varying optimization average voltage control is

$$u_{vodi} = -\beta[\nabla_{\bar{v}i\bar{v}i}\phi_{\bar{v}i}]^{-1}\left[\varepsilon\nabla_{\bar{v}i}\phi_{\bar{v}i} + \mathrm{sig}(\bar{v}_i - \bar{v}_j)^{\kappa} + \nabla_{\bar{v}i\rho}\phi_{\bar{v}i}\dot{\rho}_{\bar{v}}(t) + \nabla_{\bar{v}i\sigma i}\phi_{\bar{v}i}\dot{\sigma}_{\bar{v}i}(t) + \nabla_{\bar{v}it}\phi_{\bar{v}i}\right], \quad i \in \mathcal{G}_{fm}. \tag{34}$$

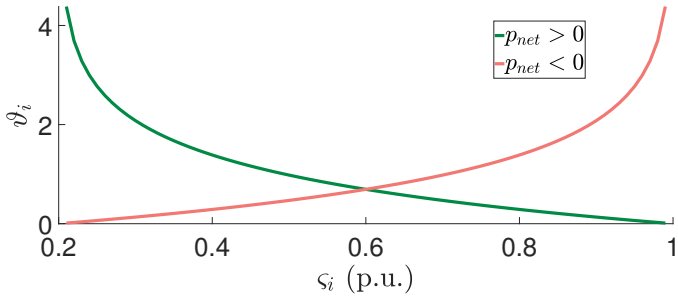

Fig. 3: Tuning gain ϑ_i for different normalized state of charge (SOC) and $p_{net} > 0$ and $p_{net} < 0$.

3) Real and Reactive Power Optimization: The real output power for the converter with connected PV and BES, which is regulated in grid forming mode, is

$$p_i = p_{pvi} + p_{besi}, i \in \mathcal{G}_{fm}, \tag{35}$$

where p_{pvi} and p_{besi} are the output power for PV and BES, respectively; and $p_{besi} > 0$ denotes the BES is discharging. Since the BES can balance the power demand, the PV can be controlled via the MPPT method, such that $p_{pvi} = p_{\mathrm{MPPT}i}$. Thus, the objective of the PV and BES converter is to reduce battery charging and discharging power and save battery lifetime. Furthermore, reactive power should also be minimized to reduce power losses resulting from reactive power balance. Therefore, the objective function for the power regulation of PV and BES converter is

$$\begin{aligned} \min_{p_{besi},\, q_i} \; & f_{\mathcal{Z}i}\left(p_{besi},\, q_i\right) = c_1 \left\|p_{besi}\right\|_2^2 + c_2 \left\|q_i\right\|_2^2, \\ & i \in \mathcal{G}_{fm}, \end{aligned} \tag{36}$$

where c_1 and c_2 are gains associated with the multi-objective function. They represent the costs of real power supply from the battery and reactive power injection, respectively. Minimizing reactive power injection can involve a trade-off with (average) voltage regulation. The gains c_1 and c_2 are tuned to balance power quality improvements with economic operation.

In addition, this paper considers cooperation among BESs to prevent overcharging and overdischarging. BESs dynamically adjust their output powers based on the net power and SOC. Specifically, in scenarios where there is a positive net power, BESs should supply power to loads, with BESs having a lower SOC supplying less power, where the net power indicates the total power demand in the μGs. Conversely, in cases of negative net power, BESs with lower SOCs will receive more power. To achieve this, a sparse constraint related to variable output power $\tilde{p}_i$ is introduced. The variable output power $\tilde{p}_i$ can be calculated as

$$\tilde{p}_i = \vartheta_i p_{besi}, i \in \mathcal{G}_{fm}, \tag{37}$$

where ϑ_i is the dynamic tuning gain to vary the output power of BES. In this paper, the logarithm-based tuning method is proposed based on the μG's net power and its SOC.

$$\begin{aligned} \vartheta_i = & -\tfrac{1}{2}\left[\operatorname{sign}\left(p_{net}\right)+1\right]\ln\left(\varsigma_i\right) \\ & -\left[1-\tfrac{1}{2}\left[\operatorname{sign}\left(p_{net}\right)+1\right]\right]\ln\left(-\varsigma_i+1\right), \\ & i \in \mathcal{G}_{fm}, \end{aligned} \tag{38}$$

where p_{net} is the μG net power; ς_i is the SOC as

$$\dot{\varsigma}_i = -\frac{p_{besi}}{E_i}, i \in \mathcal{G}_{fm}, \tag{39}$$

where, E_i is the size of the $i-$th BES in Ws. ϑ_i is further normalized as

$$\tilde{\vartheta}_i = \alpha_\vartheta \frac{\vartheta_i - \underline{\vartheta}}{\bar{\vartheta} - \underline{\vartheta}} + \beta_\vartheta, i \in \mathcal{G}_{fm}, \tag{40}$$

where, $\bar{\vartheta}$ and $\underline{\vartheta}$ are the upper and lower boundaries of all ϑ_i; α_ϑ and β_ϑ are parameters for the normalization. Fig. 3 presents the variation of ϑ_i according to the SOC level of a BES. If $p_{net} = 0$, the μG is well balanced without BESs and the BESs are idle.

The variable output power must satisfy the following sparse constraints to achieve the cooperative operation,

$$\mathcal{L}\tilde{\mathbf{p}} = \mathbf{0}, \tag{41}$$

where $\tilde{p} = \left[\begin{array}{ccccccc} \tilde{p}_1, & \cdots, & \tilde{p}_i, & \cdots, & \tilde{p}_{Nfm} \end{array}\right]^T$. The sparse constraint also indicates $\tilde{p}_i = \tilde{p}_j = \cdots$. Invoked by (37) and constraint (41), the larger ϑ_i is, the less output power is provided or absorbed by BES. (38) ensures the BES with the larger ϑ_i is in a lower SOC state under a negative net power case, and a higher SOC state under a positive net power case.

Remark 3: From (37) and (41), it follows that $\vartheta_i p_{besi} = \vartheta_j p_{besj}$ for all i, j. As shown in Fig. 3, when $p_{net} < 0$ (charging regime), a higher SOC yields a larger ϑ_i and thus a smaller charging power magnitude $|p_{besi}|$; lower-SOC units absorb more power, promoting SOC equalization.

Also, the reactive power sharing is introduced into the optimal problem as a sparse constraint,

$$\mathcal{L}\tilde{\mathbf{q}} = \mathbf{0}, \tag{42}$$

where $\tilde{\mathbf{q}} = \left[\begin{array}{ccccccc} \tilde{q}_1, & \cdots, & \tilde{q}_i, & \cdots, & \tilde{q}_{Nfl} \end{array}\right]^{\mathrm{T}}$; $\tilde{q}_i = n_i q_i$. This sparse constraint means that $\tilde{q}_i = \tilde{q}_j = \cdots$.

Despite of the above sparse constraints, the following local constraints should also be considered for the time varying optimization of power control. The real and reactive power should be maintained in the required range,

$$\begin{aligned} & p_{chri} \le p_{besi} \le p_{dchri}, \\ & -q_{\max i} \le q_i \le q_{\max i}, i \in \mathcal{G}_{fm}, \end{aligned} \tag{43}$$

where p_{chri} and p_{dchri} are the maximum charging and discharging powers of BES. $q_{\max i}$ is the maximum limit of the reactive power. Furthermore, since the real and reactive powers are coupled and constrained by the rated apparent output power of the converter,

$$\left(p_{besi} + p_{\mathrm{MPPT}i}\right)^2 + q_i^2 \le s_{rtdi}^2, i \in \mathcal{G}_{fm}, \tag{44}$$

where s_{rtdi} is the rated apparent power of the i-th converter. Also, the SOC of BES should be limited to extend the battery lifetime,

$$\underline{\varsigma} \le \varsigma_i \le \bar{\varsigma}, i \in \mathcal{G}_{fm}. \tag{45}$$

The optimal problem for real and reactive power can be summarized as

$$\begin{aligned} & \min_{p_{besi},\, q_i} f_{\mathcal{Z}i}\left(p_{besi},\, q_i,\right) \\ & \text{s.t. } \left(\mathcal{L} \otimes I_2\right)\mathcal{Z} = \mathbf{0}, \mathbf{g}_i\left(p_{besi},\, q_i\right) \le \mathbf{0}, \\ & \qquad i \in \mathcal{G}_{fm}, \end{aligned} \tag{46}$$

where $\mathbf{g}_i\left(p_{besi},\, q_i\right)$ are the constraints (43) to (45); $\mathcal{Z} = \left[\begin{array}{ccccccc} \mathcal{Z}_1^{\mathrm{T}}, & \cdots, & \mathcal{Z}_i^{\mathrm{T}}, & \cdots, & \mathcal{Z}_N^{\mathrm{T}} \end{array}\right]^{\mathrm{T}}$, and $\mathcal{Z}_i = [\tilde{p}_i,\, \tilde{q}_i]^{\mathrm{T}}$. Then, the local constraints are dealt with via a logarithmic type indicator function, similar as for the frequency control design. Thus, the modification of objective function (36) gives

$$\begin{aligned} \phi_{\mathcal{Z}i} = & f_{\mathcal{Z}i}\left(p_{besi},\, q_i\right) \\ & -\tfrac{1}{\rho_{\mathcal{Z}i}(t)}\ln\left[\sigma_{\mathcal{Z}i}\left(t\right) - g_{ij}\left(p_{besi},\, q_i\right)\right], \\ & i \in \mathcal{G}_{fm}, \end{aligned} \tag{47}$$

where $\rho_{\mathcal{Z}i} > 0$ is the indicator function parameter , $\sigma_{\mathcal{Z}i}\left(t\right)$ is a slack function for real and reactive power optimization, where $\rho_{\mathcal{Z}i}\left(t\right) = a_{\mathcal{Z}i} e^{b_{\mathcal{Z}i} t}$, and $\rho_{\mathcal{Z}i}\left(t\right) = c_{\mathcal{Z}i} e^{-d_{\mathcal{Z}i} t}$ with $a_{\mathcal{Z}i} >$

$0,\ b_{\mathcal{Z}i} > 0,\ c_{\mathcal{Z}i} > 0,$ and $d_{\mathcal{Z}i} > 0$. Therefore, the Lagrangian of the real and reactive power optimization problem is,

$$\mathfrak{L}_{\mathcal{Z}} = \sum_{i} \phi_{\mathcal{Z}i} + \lambda_{\mathcal{Z}}^{\mathrm{T}} \left(\mathcal{L} \otimes I_2\right) \mathcal{Z}, i \in \mathcal{G}_{fm}, \tag{48}$$

where $\lambda_{\mathcal{Z}}$ is the Lagrange multiplier for the sparse real and reactive power sharing constraints. Following a similar design procedure, the distributed secondary time varying optimization control for real and reactive power regulation is,

$$\begin{aligned} u_{\mathcal{Z}i} = &-\left[\nabla_{\mathcal{Z}i\mathcal{Z}i}\phi_{\mathcal{Z}i}\right]^{-1}\left[\varepsilon\nabla_{\mathcal{Z}i}\phi_{\mathcal{Z}i} + \mathrm{sig}(\mathcal{Z}_i - \mathcal{Z}_j)^{\kappa}\right. \\ &\left.+\nabla_{\mathcal{Z}i\rho}\phi_{\mathcal{Z}i}\dot{\rho}_{\mathcal{Z}i}\left(t\right) + \nabla_{\mathcal{Z}i\sigma}\phi_{\mathcal{Z}i}\dot{\sigma}_{\mathcal{Z}i}\left(t\right) + \nabla_{\mathcal{Z}it}\phi_{\mathcal{Z}i}\right], \\ i \in \mathcal{G}_{fm}, \end{aligned} \tag{49}$$

where $u_{\mathcal{Z}i} = \left[u_{pi},\ u_{qi}\right]^{\mathrm{T}}$.

C. Distributed Time Varying Optimization for Photovoltaic Systems

The converter with only a connected PV source will work in the GFM. In this case, the secondary reactive power control objective is same as for the PV and BES converter. The real power optimization objective is tracking the MPPT output power such that,

$$\begin{aligned} &\min_{p_{pvi},\ q_i} f_{pvi}\left(p_{pvi},\ q_i\right) = c_{pv1}\left\|p_{pvi} - p_{\mathrm{MPPT}i}\right\|_2^2 + c_{pv2}\left\|q_i\right\|_2^2, \\ &i \in \mathcal{G}_{fl}, \end{aligned} \tag{50}$$

where c_{pv1} and c_{pv2} are gains for the multi-objectives of the PV system alone. For real power regulation, the cooperative principle requires that all PV-only converters track the same MPPT output power. Thus, there is

$$p_{pvi}/p_{\mathrm{MPPT}i} = p_{pvj}/p_{\mathrm{MPPT}j} = \cdots, i \in \mathcal{G}_{fl}. \tag{51}$$

Rewriting the above constraint into a sparse form gives,

$$\mathcal{L}\widehat{\mathbf{p}} = \mathbf{0}, \tag{52}$$

where $\widehat{\mathbf{p}} = \left[\ \widehat{p}_1,\ \cdots,\ \widehat{p}_i,\ \cdots,\ \widehat{p}_{N_{PV}}\ \right]^{\mathrm{T}}$; $\widehat{p}_i = p_{pvi}/p_{\mathrm{MPPT}i}$ and $p_{\mathrm{MPPT}i} > 0$. The real power and apparent output power constraints are,

$$\begin{aligned} &0 < p_{pvi} \le p_{\mathrm{MPPT}i}, \\ &-q_{\max i} \le q_i \le q_{\max i}, \\ &p_{pvi}^2 + q_i^2 \le s_{rtdi}^2, i \in \mathcal{G}_{fl}, \end{aligned} \tag{53}$$

Besides, the sparse constraint for reactive power sharing is the same as in (42). Thus, the optimal problem for the PV converter agent is,

$$\begin{aligned} &\text{obj. (50)}, \\ &\text{s.t. (42), and (52), sparse constraints,} \\ &\text{(53), local constraints.} \end{aligned} \tag{54}$$

Then, implementing (47) to the optimal problem (54) gives the modified objective function with the indicator function. After that, following the similar procedure for (48) and (49) gives the Lagrangian and control inputs for the distributed secondary time varying power optimization control of PV converter agents.

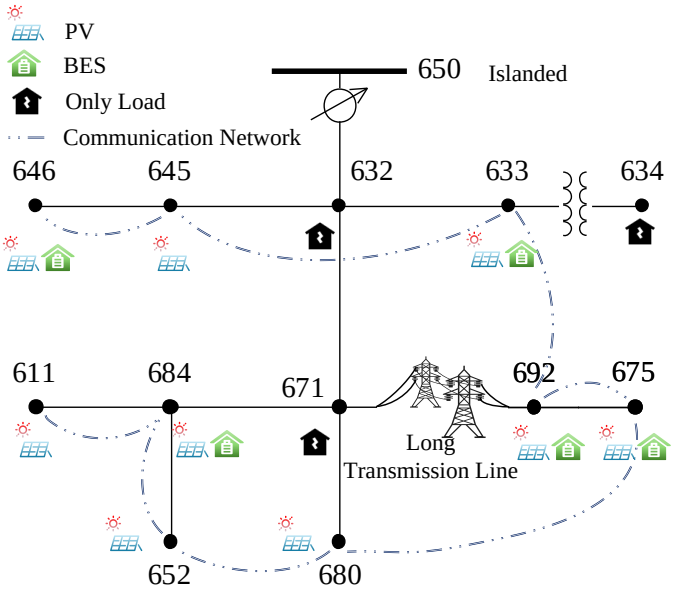

Fig. 4: Modified IEEE 13 nodes test feeder with distributed PVs and BESs.

D. Distributed Time Varying Optimization for Battery Energy Storage Systems

The time varying optimization problem for the converter agent with only BES is similar to one with the PV and BES converter by setting $p_{pvi} = p_{\mathrm{MPPT}i} = 0$. Therefore, the substitution of $p_{\mathrm{MPPT}i} = 0$ into (44) and implementation of (49) gives the distributed secondary time varying power optimization control for BES converter agents.

E. Cooperation of Heterogeneous Energy Sources

The secondary control system for different energy source systems is derived by implementing the proposed distributed secondary continuous time-varying optimization controllers for frequency regulation (25), voltage restoration (30), average voltage control (34), and real and reactive power sharing (49) into (7) or (9), based on the type of energy source system and its primary control mode, respectively. In summary, energy source systems with BES typically provide primary frequency and voltage references, while systems with stochastic sources like PV primarily operate in MPPT mode and allocate part of their capacity to assist in frequency and voltage regulation. Within BES-connected systems, efforts are made to maintain a balanced SOC. The overall configuration of the proposed continuous time-varying optimization control system is presented in Fig. 1. As shown in Fig. 1, the secondary control framework uses feedback linearization to form unified virtual inputs for heterogeneous energy sources that interface with the distributed continuous time-varying optimization layer. The optimization layer remains time-varying and can include nonlinear constraints, e.g., apparent-power limits. These constraints are handled by an interior-point method within a distributed, continuous-time optimizer that computes the control inputs online. In summary, the primary droop control dynamics for heterogeneous energy sources are linearized for

This article has been accepted for publication in IEEE Transactions on Power Systems. This is the author's version which has not been fully edited and content may change prior to final publication. Citation information: DOI 10.1109/TPWRS.2025.3629155

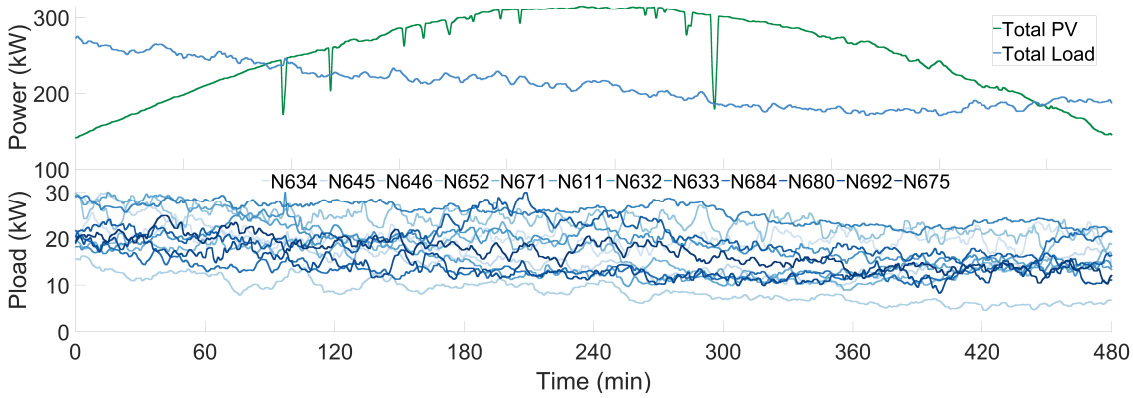

Fig. 5: PV output powers under maximum power point tracking. PV data was sourced from the NREL Baseline Measurement Station in Colorado. The zoomed-in sub-figure illustrates the PV output power between 315.6 and 316.6 minutes.

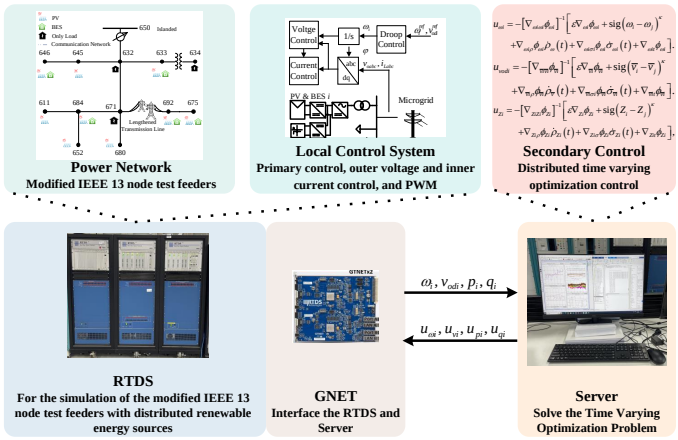

Fig. 6: RTDS setup set up to verify the proposed distributed time-varying optimization method by controlling a modified IEEE 13-node test feeder μG. The simulation was conducted using RTDS with hardware-in-the-loop. In this setup, the switch model of converters, PV and BES sources, power network, primary, and lower-level control were simulated on two RTDS racks. The proposed secondary control system was solved by a server PC, which communicated with the RTDS racks via a GNET card using the TCP/IP protocol. The required state variables for the secondary control and time-varying optimization control signals were transmitted accordingly.

the secondary control design, while the optimization problem is solved with appropriate nonlinear constraint handling.

IV. Results

The proposed distributed continuous time-varying optimization control framework was validated using an islanded IEEE 13-node test feeder with distributed PVs and BESs, as depicted in Fig. 4. Node 650 was disconnected from the main grid to form an islanded μG. In the modified IEEE 13-node μG setup, nodes 645, 611, 652, and 680 are connected only to PVs, while nodes 646, 633, 684, 692, and 675 are connected to both PVs and BESs. The VSCs have a nominal output voltage of

TABLE I: Case Study Parameters

v_{nrm}	415V	ω_{nrm}	$2\pi \times 50 rad/s$	E_i	80kWh
m_i	2.1×10^{-5}	n_i	2.5×10^{-4}	κ	0.9
ϵ	1	c_1	1	c_2	1
β	15	$\bar{\varsigma}$	1	$\underline{\varsigma}$	0.2
$a_{\omega i}$	1	$b_{\omega i}$	0.1	$c_{\omega i}$	10
$d_{\omega i}$	0.01	c_{pv1}	1	c_{pv2}	1
a_{vi}	1	b_{vi}	0.1	c_{vi}	10
d_{vi}	0.01	$a_{\mathcal{Z}i}$	1	$b_{\mathcal{Z}i}$	0.1
$c_{\mathcal{Z}i}$	10	$d_{\mathcal{Z}i}$	0.01	s_{rtdi}	200kW
p_{dchri}	80kW	p_{chri}	80kW	$q_{\max i}$	150kVar

415V, and the μG frequency is set at 50Hz. Fig. 5 illustrates PV output powers under MPPT. The PV output power data is sourced from the NREL Baseline Measurement Station in Colorado, calculated based on solar irradiance and temperature data. The output power of the PV systems ranges from 15 kW to 55 kW, increasing in 5 kW increments between Nodes 680 and 646. The batteries have a capacity of 80 kWh. The parameters for the following case studies are detailed in Table I.

The RTDS setup for simulating the μG with the proposed time-varying optimization control is depicted in Fig. 6. The simulation is conducted using the hardware-in-loop method, where a server connected to RTDS via a GNET card solves the time-varying optimization control problem.

A. Case Study A: Distributed Time Varying Optimization Control with Local Voltage Control

In this case study, distributed frequency control (25) and time-varying optimization of real and reactive power (49) or (54) are implemented as secondary controls. Additionally, a local voltage control system (30) is utilized. As shown in Fig. 4, nodes 646, 633, 684, 692, and 675 are managed using the grid forming method, which employs power control (49), with (7) facilitating the interaction between the primary and secondary control systems. In contrast, nodes 645, 611, 652, and 680 are regulated by the grid following mode, which utilizes power control (54) and primary control references set

This article has been accepted for publication in IEEE Transactions on Power Systems. This is the author's version which has not been fully edited and content may change prior to final publication. Citation information: DOI 10.1109/TPWRS.2025.3629155

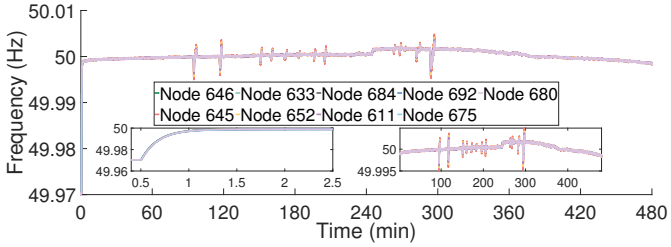

(a) Frequency

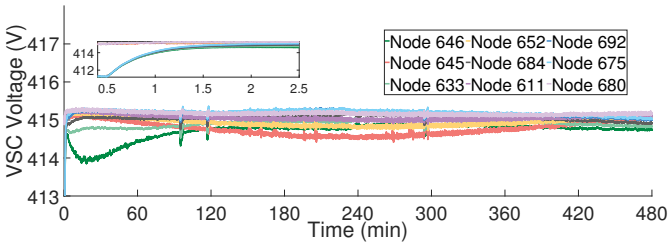

(b) Voltage

Fig. 7: Frequency and output voltage of VSCs with the local voltage control.

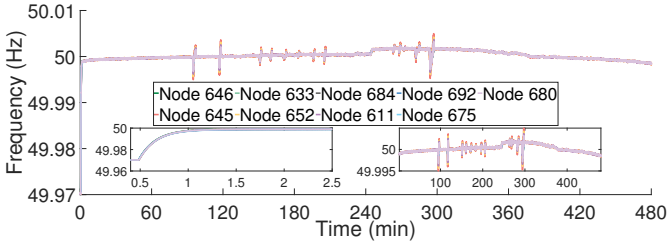

(a) Frequency

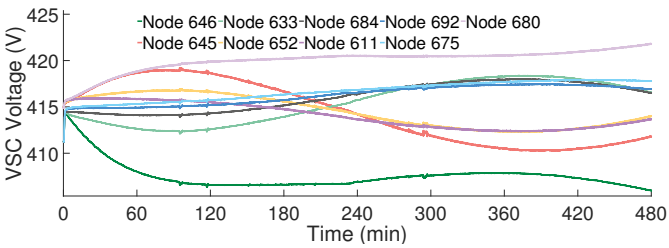

(b) Voltage

Fig. 10: Frequency and output voltage of VSCs with the local voltage control.

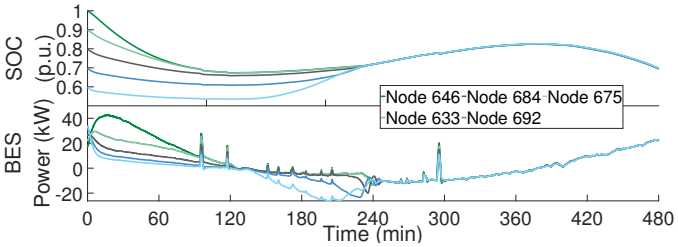

Fig. 8: Battery output powers and SOCs with the local voltage control.

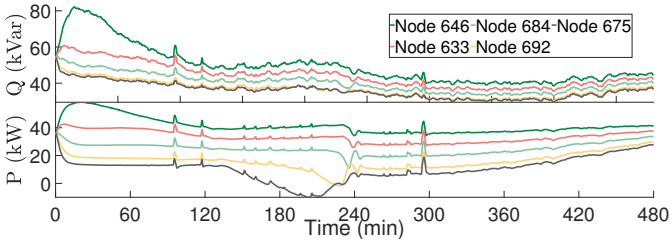

(a) Real power output of VSCs with grid forming mode

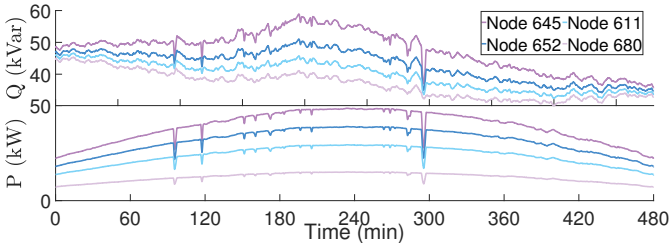

(b) Reactive power output of VSCs with grid following mode

Fig. 9: Output real and reactive powers of VSCs with the local voltage control: (a) grid forming; (b) grid following.

by (9). The real-time simulation results are presented in Figs. 7 to 9.

Fig. 7 shows the frequency and voltage of the μG under the proposed time-varying optimization. The zoomed-in sub-figure indicates that once the secondary control is activated, frequency and voltage deviations are eliminated within a short period of time. Despite rapid variations in PV output power, both voltage and frequency remain stable within a narrow range around their nominal set points.

Fig. 8 illustrates the battery output powers and SOCs. Using the battery cooperation method outlined in (37) to (41), the batteries adjust their output powers based on their SOCs and the net power of the μG. Specifically, batteries with a higher SOC discharge more power in positive net power scenarios and charge less in negative net power situations, gradually equalizing their SOC levels.

Fig. 9 displays the real and reactive power outputs of the converters. During the first 60 minutes, the BESs with higher SOC levels provide additional output power, fulfilling the real power control objectives illustrated in Fig. 3. Reactive power sharing is influenced by the trade-off between accurate voltage regulation and reactive power distribution.

From Fig. 9 , at approximately 90 minutes, PV output powers drop sharply at nodes 611, 645, 652, 680, 633, 675, 684, and 692. To maintain power balance and system frequency, BES units at nodes 633, 675, 684, and 692 increase their output. Under droop control, such imbalances manifest as frequency deviations. The proposed time-varying optimization commands the BES units to compensate for the mismatch, thereby stabilizing μG operation.

B. Case Study B: Distributed Time Varying Optimization Control with Average Voltage Control

In this case, the parameters are the same as in Case Study A, but the distributed time varying optimization of voltage is changed to (34). The simulation results of frequency and VSC output voltages, the average estimation of voltages is presented

This article has been accepted for publication in IEEE Transactions on Power Systems. This is the author's version which has not been fully edited and content may change prior to final publication. Citation information: DOI 10.1109/TPWRS.2025.3629155

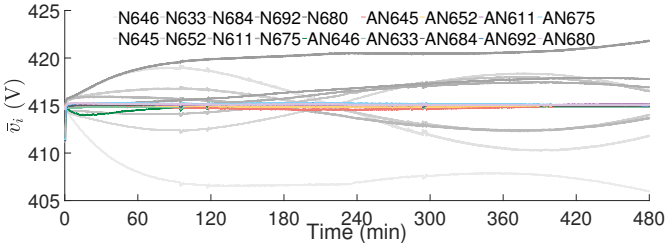

Fig. 11: Average estimation of the voltages. The sub-figure on the left shows the voltages when the distributed secondary time-varying optimization control is switched on, up to 1 minute. The sub-figure on the right illustrates the voltages from 1 to 720 minutes.

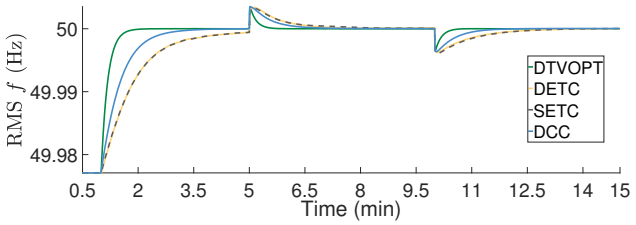

(a) Frequency

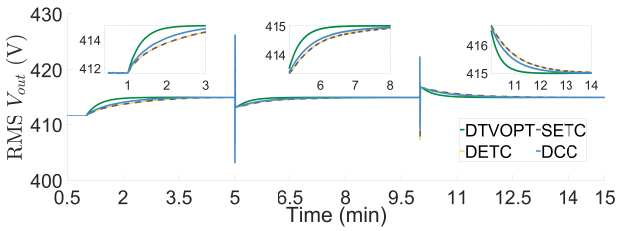

(b) Voltage

Fig. 12: Comparison studies for frequency and voltage control during loads variations.

in Fig. 10. From Fig. 10, the voltage is maintained within the required range, while the average voltage is controlled to the nominal value.

C. Case Study C: Comparisons

The proposed continuous time-varying optimization control method is compared with existing distributed control methods, specifically distributed dynamic/static event-triggered control [47] and distributed cooperative control [48]. These methods are evaluated for voltage and frequency regulation on the same power system configuration as in Case Study A, which includes nine battery energy storage systems. As shown in Fig. 12, the proposed time-varying control method demonstrates shorter settling time and faster response over the other methods during load variations.

The proposed distributed, continuous-time secondary controller enhances dynamic response, tightens frequency and voltage regulation, improves tracking accuracy, and reduces operating cost when economic terms are included. Because updates are computed locally and exchanged only with neighbors, the method is computationally efficient and well suited

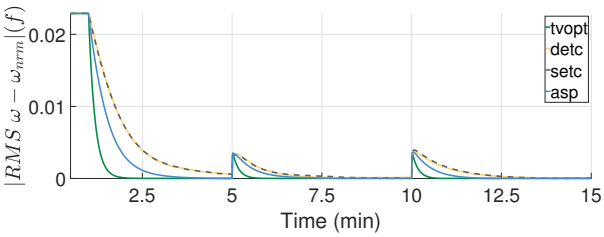

(a) Frequency

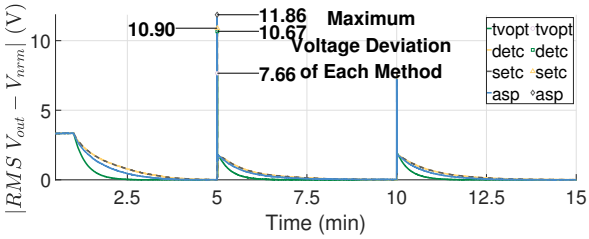

(b) Voltage

Fig. 13: RMS errors of frequency and voltage control during loads variations for comparisons.

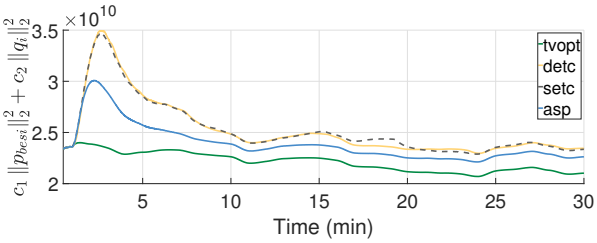

Fig. 14: Comparison studies for the cost functions (36).

to heterogeneous μGs subject to rapid renewable and load variations.

The controller yields faster transients and shorter settling times, thereby improving power quality. As shown in Fig. 13, both frequency and voltage RMS errors are lower than with existing schemes, indicating tighter regulation and higher reliability. In particular, Fig. 13b, the maximum voltage deviation is limited to 7.66V, reducing the risk of violating voltage limits during large disturbances such as abrupt renewable losses or load steps.

Fig. 14 further compares the cost in (36). The proposed approach consistently achieves a lower cumulative cost than benchmark controllers, reflecting more efficient battery dispatch and reduced reactive power effort.

D. Case Study D: Modified IEEE 37 Test Feeder Distributed with Renewable Energy Sources and Energy Storage System and Operated in an Islanded Mode

This case study demonstrates the adaptability and scalability of the proposed method on a larger benchmark system. A modified islanded IEEE 37-bus feeder with distributed PV and BES resources was implemented on RTDS with hardware-in-the-loop control to validate the distributed time-varying optimization framework. Secondary frequency

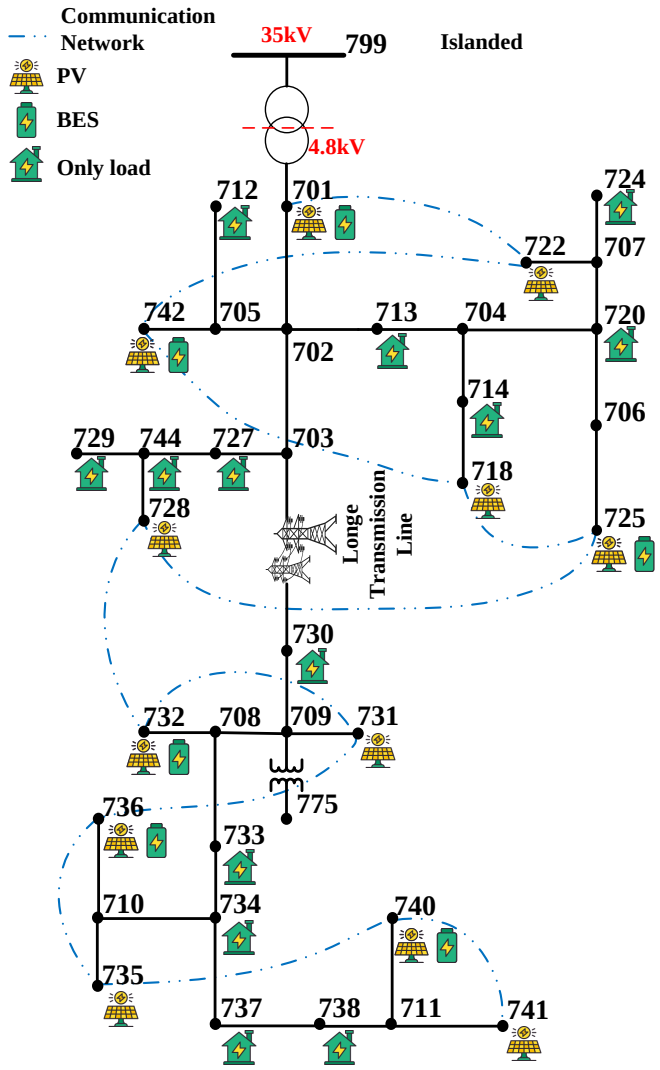

Fig. 15: Modified IEEE 37 nodes test feeder with distributed PVs and BESs.

control (25), real/reactive power optimization (49) (or (54) for PV-only units), and local voltage control (30) were deployed. As shown in Fig. 15, nodes 701, 742, 725, 732, 736, and 740 operate in grid-forming mode using (49) with references generated via (7); nodes 722, 718, 728, 731, 735, and 741 operate in grid-following mode using (54) with references from (9).

Figs. 16a and 16b show that frequency and voltage remain tightly regulated within the prescribed limits (±0.2Hz and ±20.075V; bounds illustrated in Fig. 17) despite renewable variability. Fig. 18 confirms all BES SOC trajectories stay within their allowable range while the cooperative sharing rule (37) maintains SOC balance. Real and reactive power behaviors for grid-forming and grid-following converters are shown in Figs. 19a and 19b. In Fig. 19a the real power reflects combined PV plus BES contributions, whereas in Fig. 19b the real power originates solely from PV units. These results verify correct coordination, constraint adherence, and scalability of the distributed continuous time-varying optimization approach on a larger heterogeneous μG.

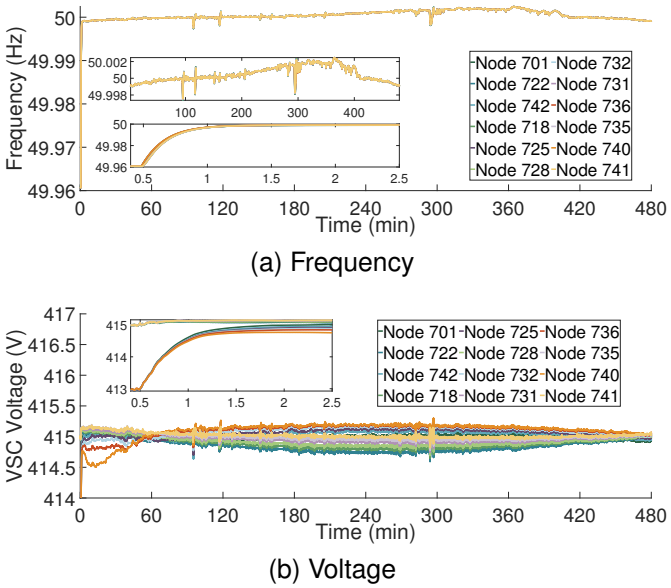

Fig. 16: Frequency and output voltage of VSCs with the local voltage control.

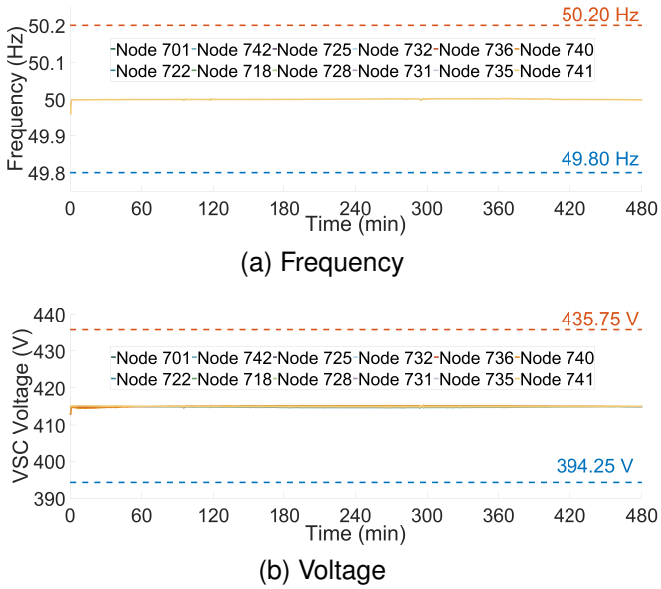

Fig. 17: Frequency, output voltage and their upper and lower limitations of VSCs with the local voltage control.

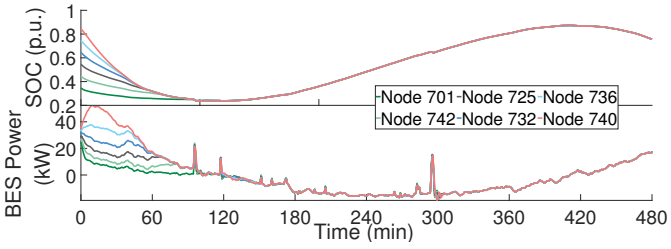

Fig. 18: Battery output powers and SOCs with the local voltage control.

E. Case Study E: Impact of Communication Delay, Packet Loss, and Measurement Noise

In this case study, we evaluate the impact of communication impairments—time delay, packet loss, and measurement

This article has been accepted for publication in IEEE Transactions on Power Systems. This is the author's version which has not been fully edited and content may change prior to final publication. Citation information: DOI 10.1109/TPWRS.2025.3629155

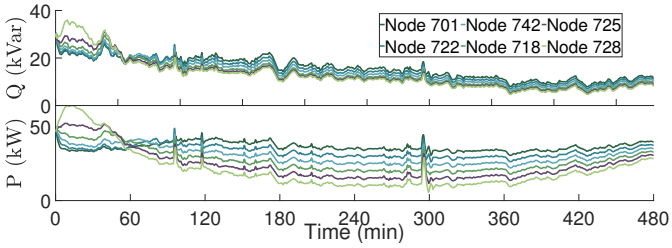

(a) Real power output of VSCs with grid forming mode

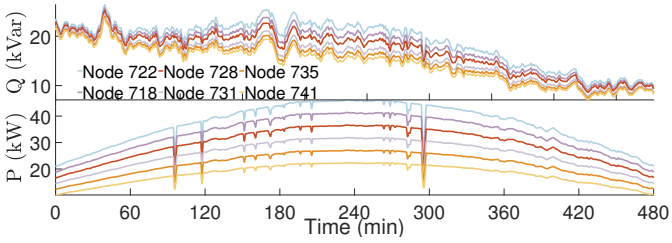

(b) Reactive power output of VSCs with grid following mode

Fig. 19: Output real and reactive powers of VSCs with the local voltage control: (a) grid forming; (b) grid following.

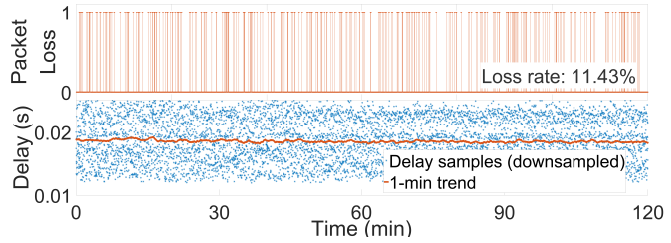

Fig. 20: Packet loss and time delay during the communication.

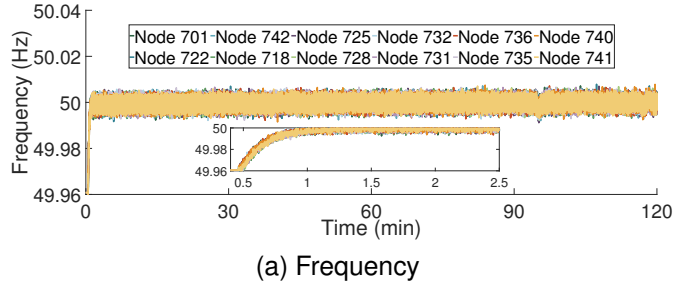

(a) Frequency

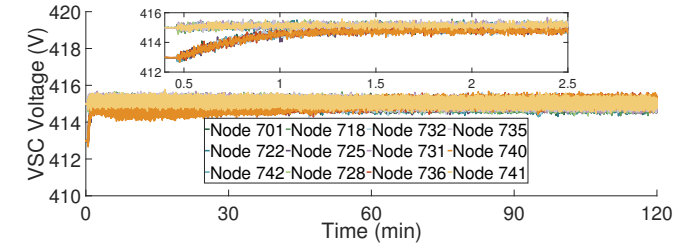

(b) Voltage

Fig. 21: Frequency and output voltage of VSCs under local voltage control, including measured noise and packet loss effects during communication. Upper and lower operational limits are indicated.

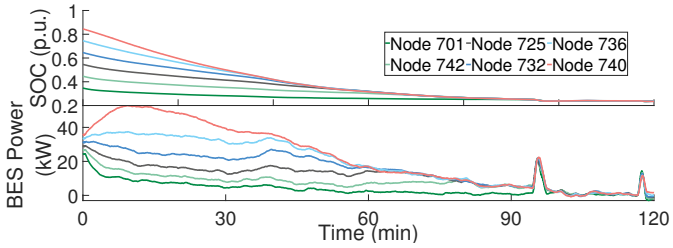

Fig. 22: Battery output powers and SOCs with the local voltage control, including measured noise and packet loss effects during communication.

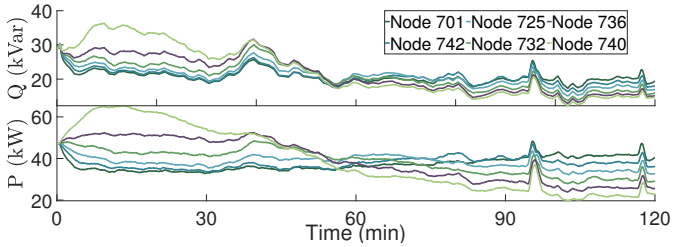

(a) Real power output of VSCs with grid forming mode

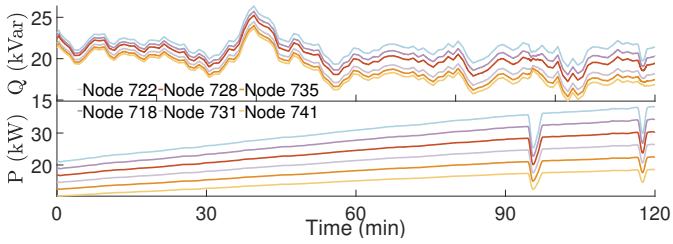

(b) Reactive power output of VSCs with grid following mode

Fig. 23: Output real and reactive powers of VSCs with the local voltage control: (a) grid forming; (b) grid following, including measured noise and packet loss effects during communication.

noise—using the same benchmark as Case Study D. Gaussian white noise (mean 0, variance 1.04×10^{-2} to 1.25) is added to RTDS state measurements; random packet loss of 10% is imposed on the communication links; and time delay arises from data transfer between RTDS and the server. The realized packet loss and delay are shown in Fig. 20: a value of 1 indicates a dropped packet and 0 indicates successful transmission. The downsampled delay trace (red line) indicates an average delay of about 0.02s.

Figs 21–23 show that frequency and voltage remain stable and within the prescribed limits despite these impairments. Battery power and SOC trajectories, Fig. 22, governed by the cooperative sharing rule (37) maintains SOC balance. Real and reactive power outputs, Fig. 23, exhibit only minor deviations, with overall trends consistent with Case Study D. These results demonstrate that the proposed distributed continuous time-varying optimization framework is robust to realistic noise, delay, and packet loss in the communication network.

Remark 4: In the case studies, the μG and all primary and lower-level controllers are modeled on the RTDS, Real-Time Digital Simulator. The proposed secondary, time-varying opti-

mization runs on a dedicated server in a hardware-in-the-loop configuration.

The secondary controller exchanges data with RTDS over TCP/IP via the GNET interface. At each sampling instant, RTDS streams measurements to the server; the server updates and solves the optimization and returns converter setpoints. RTDS applies these setpoints immediately, closing the HIL loop.

This setup offers three advantages:

1) High-fidelity dynamics are achieved because switching-level converter models and a nonlinear battery model capture fast transients under realistic conditions.
2) Efficient execution is ensured by running the complex optimization on external hardware with deterministic timing, while RTDS focuses on real-time network and renewable energy source device simulation.
3) Realism is preserved because the architecture mirrors deployments in which local devices receive setpoints from a supervisory controller over a communication link.

A limitation is scalability of the VSCs on the RTDS setup. i.e. detailed converter models typically occupy dedicated RTDS processor cores, so the size and node count of the simulated system are bounded by available hardware.

Possible future work on the piratical implementation of the proposed distributed time varying optimization control framework includes:

1) Design industrial-grade control hardware with appropriate communication interfaces.
2) Port and tune the time-varying optimizer on this hardware to meet real-time deadlines.
3) Integrate and validate data exchange so that only sampled measurements and optimized setpoints are transmitted.

V. Conclusion

This paper presented a distributed continuous time-varying optimization framework for secondary μG control, unifying frequency and voltage restoration with adaptive real/reactive power sharing across heterogeneous grid forming and grid following converters. The feedback-linearized secondary layer exposes heterogeneous energy source dynamics that are driven by continuous-time optimal controllers subject to local and consensus constraints, including PV maximum power point tracking variability and frequency and voltage limits, and so on. Real-time hardware-in-the-loop studies on a modified IEEE 13-node feeder verified stable operation with both local and average voltage objectives.

Quantitatively, the proposed approach reduced frequency and voltage RMS regulation errors relative to benchmark distributed secondary controllers, limited the worst-case voltage excursion during large load and renewable perturbations, and lowered the cumulative multi-objective operating cost, while maintaining SOC balance for all BESs. A larger islanded IEEE 37-node case further demonstrated scalability, heterogeneous coordination, and constraint adherence under mixed grid forming/grid following operation.

Appendix A
Implementation of Feedback Linearization for Secondary Control Framework

Feedback linearization transforms a dynamic system into decoupled linear dynamics by designing the feedback input. It makes explicit the mapping between control inputs and system states required by the secondary controller. In this work, the secondary layer builds on primary droop control, which couples frequency with real power and voltage with reactive power, respectively. For each channel, the necessary input–state relation is derived. The procedure is illustrated below using the frequency–power droop as an example.

Take the derivative of (1),

$$\dot{\omega}_i = \dot{\omega}_i^{ref} - m_i \dot{p}_i. \tag{55}$$

The secondary control is proposed for grid forming converter with frequency - power droop control to eliminate the frequency deviation and to provide a accurate power sharing among converters. Thus, the frequency control and power control inputs should be designed, which is defined as $u_{\omega i}$, and u_{pi}, respectively. Thus, there is

$$\dot{\omega}_i = u_{\omega i},\ m_i \dot{p}_i = u_{pi}. \tag{56}$$

The dynamic of new state is:

$$\dot{\omega}_i^{ref} = \dot{\omega}_i + m_i \dot{p}_i = u_{\omega i} + u_{pi} = \mathcal{V}_i, \tag{57}$$

where, $\mathcal{V}_i$ is the new feedback input.

For grid-following units, applying the same procedure to the p–f and q–v droops produces linear maps for p_i^{ref} and q_i^{ref}, consistent with (9). In summary, feedback linearization provides unified virtual inputs that the distributed time-varying optimizer computes in real time and that are then integrated to generate the primary references as in (7) and (9).

Appendix B
Proofs of Stabilities of the Distributed Time Varying Optimization Control

To analysis the stability of the distributed time varying optimization control for frequency regulation, the following Lyapunov function is defined,

$$V_\omega(t) = \frac{1}{2} \left\| \nabla_\omega \sum_i \phi_{\omega i} \right\|_2^2. \tag{58}$$

Following by (19) and $\mathcal{L}^{\mathrm{T}} \lambda_\omega^* = \mathbf{0}$, $V_\omega(t) = \mathbf{0}$ with the optimal solution ω^*.

The time derivative of (58) along with the dynamics of (25) is

$$\begin{aligned}\dot{V}_\omega(t) &= \left(\nabla_\omega \sum_i \phi_{\omega i}\right)^{\mathrm{T}} \Bigg[\nabla_{\omega\omega} \sum_i \phi_{\omega i}\dot{\omega} + \nabla_{\omega\rho} \sum_i \phi_{\omega i}\dot{\boldsymbol{\rho}}_\omega(t) \\ &\quad + \nabla_{\omega\sigma} \sum_i \phi_{\omega i}\dot{\boldsymbol{\sigma}}_\omega(t) + \nabla_{\omega t} \sum_i \phi_{\omega i} \\ &\quad - \sum_i \sum_{j\in\mathcal{N}_i} \mathrm{sig}(\omega_i - \omega_j)^\kappa \Bigg] \\ &= \left(\nabla_\omega \sum_i \phi_{\omega i}\right)^{\mathrm{T}} \Bigg[- \beta\varepsilon \sum_i \nabla_\omega \phi_{\omega i} \\ &\quad - \sum_i \sum_{j\in\mathcal{N}_i} \mathrm{sig}\left(\omega_i - \omega_j\right)^\kappa \Bigg] \\ &\leq -\beta\varepsilon \left(\nabla_\omega \sum_i \phi_{\omega i}\right)^{\mathrm{T}} \sum_i \nabla_\omega \phi_{\omega i} \\ &= -2\beta\varepsilon V_\omega(t),\end{aligned} \tag{59}$$

which implies $\nabla_\omega \sum_i \phi_{\omega i}$ exponentially converges to 0. Then, implementation of mean-value theorem to $\nabla_\omega \sum_i \phi_{\omega i}$ gives,

$$\nabla_\omega \sum_i \phi_{\omega i} = \nabla_{\omega\omega} \sum_i \phi_{\omega i}\left(\eta_i\right)\left(\omega_i - \omega_i^*\right), \tag{60}$$

where, $\eta_i = \omega_i^* + \tau\left(\omega_i - \omega_i^*\right)$ is a convex combination of ω_i and ω_i^*. Invoked by (17), $\phi_{\omega i}$ is of strong convexity and there is $\left\|\nabla_{\omega\omega} \sum_i \phi_{\omega i}\left(\eta_i\right)\right\|_2 \leq M_{\phi\omega}$. After that, with the Cauchy-Shwartz inequality, there is,

$$\left\|\omega - \omega^*\right\|_2 \leq M_{\phi\omega}^{-1} \left\|\nabla_\omega \sum_i \phi_{\omega i}\right\|_2. \tag{61}$$

Then, invoked by (59), $V_\omega(t) \leq e^{-2\beta\varepsilon t} V_\omega(t)|_{t=0}$ is held. Equivalently, following inequality can be obtained.

$$\left\|\nabla_\omega \sum_i \phi_{\omega i}\right\|_2 \leq e^{-\beta\varepsilon t} \left\|\nabla_\omega \sum_i \phi_{\omega i}\,|_{t=0}\right\|_2. \tag{62}$$

Thus, there is

$$\begin{aligned}\lim_{t\to\infty} \left\|\omega - \omega^*\right\|_2 &\leq \lim_{t\to\infty} M_{\phi\omega}^{-1} \left\|\nabla_\omega \sum_i \phi_{\omega i}\right\|_2 \\ &\leq \lim_{t\to\infty} M_{\phi\omega}^{-1} e^{-\beta\varepsilon t} \left\|\nabla_\omega \sum_i \phi_{\omega i}\Big|_{t=0}\right\|_2 \\ &= 0,\end{aligned}$$

which indicates the dynamics with the distributed time varying frequency control of (25) can achieve the solution of the optimal problem with the objective function (17).

REFERENCES

[1] T. Morstyn, B. Hredzak, and V. G. Agelidis, "Control strategies for microgrids with distributed energy storage systems: An overview," *IEEE Transactions on Smart Grid*, vol. 9, no. 4, pp. 3652–3666, 2018.

[2] T. Patel and P. Chauhan, "Pre-synchronization of weak source in microgrid," *IEEE Transactions on Power Electronics*, pp. 1–6, 2024.

[3] M. M. H. Sifat and S. K. Das, "Proactive and reactive maintenance strategies for self-healing digital twin islanded microgrids using fuzzy logic controllers and machine learning techniques," *IEEE Transactions on Power Systems*, pp. 1–10, 2024.

[4] W. Du, F. K. Tuffner, K. P. Schneider, R. H. Lasseter, J. Xie, Z. Chen, and B. Bhattarai, "Modeling of grid-forming and grid-following inverters for dynamic simulation of large-scale distribution systems," *IEEE Transactions on Power Delivery*, vol. 36, no. 4, pp. 2035–2045, 2021.

[5] T. Shi, X. Xiang, J. Lei, B. Liu, F. Wang, H. Yang, L. Li, and W. Li, "Communication-less active damping method with vsc for stability improvement of grid-connected dc microgrid with selected frequency islanding detection," *IEEE Transactions on Industrial Electronics*, pp. 1–11, 2024.

[6] S. Kiani, A. Salmanpour, M. Hamzeh, and H. Kebriaei, "Learning robust model predictive control for voltage control of islanded microgrid," *IEEE Transactions on Automation Science and Engineering*, pp. 1–12, 2024.

[7] T. Morstyn, B. Hredzak, and V. G. Agelidis, "Control strategies for microgrids with distributed energy storage systems: An overview," *IEEE Transactions on Smart Grid*, vol. 9, no. 4, pp. 3652–3666, 2018.

[8] W. Du, F. K. Tuffner, K. P. Schneider, R. H. Lasseter, J. Xie, Z. Chen, and B. Bhattarai, "Modeling of grid-forming and grid-following inverters for dynamic simulation of large-scale distribution systems," *IEEE Transactions on Power Delivery*, vol. 36, no. 4, pp. 2035–2045, 2021.

[9] A. Hoke, R. Mahmud, A. Nelson, D. Pattabiraman, M. Asano, D. Arakawa, B. Pierre, M. Elkhatib, J. Tan, V. Gevorgian, C. Antonio, and E. Ifuku, "Fast grid frequency support from distributed energy resources," 2021.

[10] A. Singhal, T. L. Vu, and W. Du, "Consensus control for coordinating grid-forming and grid-following inverters in microgrids," *IEEE Transactions on Smart Grid*, vol. 13, no. 5, pp. 4123–4133, 2022.

[11] A. Askarian, J. Park, and S. Salapaka, "Enhanced grid-following (e-gfl) inverter: A unified control framework for stiff and weak grids," *IEEE Transactions on Power Electronics*, vol. 39, no. 5, pp. 5089–5107, 2024.

[12] X. Gong and X. Wang, "A novel koopman-inspired method for the secondary control of microgrids with grid-forming and grid-following sources," *Applied Energy*, vol. 333, p. 120631, 2023.

[13] C. Zhang, X. Dou, L. Wang, Y. Dong, and Y. Ji, "Distributed cooperative voltage control for grid-following and grid-forming distributed generators in islanded microgrids," *IEEE Transactions on Power Systems*, vol. 38, no. 1, pp. 589–602, 2023.

[14] S. Chakraborty, S. Patel, and M. V. Salapaka, "μ-synthesis-based generalized robust framework for grid-following and grid-forming inverters," *IEEE Transactions on Power Electronics*, vol. 38, no. 3, pp. 3163–3179, 2023.

[15] J. Hu, Y. Shan, Y. Yang, A. Parisio, Y. Li, N. Amjady, S. Islam, K. W. Cheng, J. M. Guerrero, and J. Rodríguez, "Economic model predictive control for microgrid optimization: A review," *IEEE Transactions on Smart Grid*, vol. 15, no. 1, pp. 472–484, 2024.

[16] A. Simonetto, E. Dall'Anese, S. Paternain, G. Leus, and G. B. Giannakis, "Time-varying convex optimization: Time-structured algorithms and applications," *Proceedings of the IEEE*, vol. 108, no. 11, pp. 2032–2048, 2020.

[17] J. Leithon, S. Sun, and T. J. Lim, "Demand response and renewable energy management using continuous-time optimization," *IEEE Transactions on Sustainable Energy*, vol. 9, no. 2, pp. 991–1000, 2018.

[18] S. Rahili and W. Ren, "Distributed continuous-time convex optimization with time-varying cost functions," *IEEE Transactions on Automatic Control*, vol. 62, no. 4, pp. 1590–1605, 2017.

[19] A. Simonetto, A. Koppel, A. Mokhtari, G. Leus, and A. Ribeiro, "Decentralized prediction-correction methods for networked time-varying convex optimization," *IEEE Transactions on Automatic Control*, vol. 62, no. 11, pp. 5724–5738, 2017.

[20] Y. Yue and Q. Liu, "Distributed predefined-time convergent algorithm for solving time-varying resource allocation problem over directed networks," *IEEE Transactions on Cybernetics*, vol. 55, no. 5, pp. 2463–2473, 2025.

[21] X. Yi, X. Li, L. Xie, and K. H. Johansson, "Distributed online convex optimization with time-varying coupled inequality constraints," *IEEE Transactions on Signal Processing*, vol. 68, pp. 731–746, 2020.

[22] N. Bastianello, A. Simonetto, and R. Carli, "Prediction-correction splittings for time-varying optimization with intermittent observations," *IEEE Control Systems Letters*, vol. 4, no. 2, pp. 373–378, 2020.

[23] R. Dixit, A. S. Bedi, R. Tripathi, and K. Rajawat, "Online learning with inexact proximal online gradient descent algorithms," *IEEE Transactions on Signal Processing*, vol. 67, no. 5, pp. 1338–1352, 2019.

[24] A. Simonetto, J. Monteil, and C. Gambella, "Real-time city-scale ridesharing via linear assignment problems," *TRANSPORTATION RESEARCH PART C-EMERGING TECHNOLOGIES*, vol. 101, pp. 208–232, APR 2019.

[25] V. Trovato, "System scheduling with optimal time-varying delivery intervals for frequency response," *IEEE Transactions on Power Systems*, vol. 37, no. 6, pp. 4270–4285, 2022.

[26] J. Wu, M. Liu, W. Lu, K. Xie, and M. Xie, "Time-varying tracking algorithm for active distribution grid energy management considering uncertainty of feeder parameters," *CSEE Journal of Power and Energy Systems*, pp. 1–10, 2023.

[27] X. Zhu, X. Hou, J. Li, G. Yan, C. Li, and D. Wang, "Distributed online prediction optimization algorithm for distributed energy resources considering the multi-periods optimal operation," *Applied Energy*, vol. 348, p. 121612, 2023.

[28] W. Lu, K. Xie, M. Liu, X. Wang, and L. Cheng, "Online decentralized tracking for nonlinear time-varying optimal power flow of coupled transmission–distribution grids," *IEEE Transactions on Power Systems*, vol. 39, no. 2, pp. 2706–2722, 2024.

[29] E. Dall'Anese and A. Simonetto, "Optimal power flow pursuit," *IEEE Transactions on Smart Grid*, vol. 9, no. 2, pp. 942–952, 2018.

[30] Q. Wang, S. Huang, L. Xiong, Y. Zhou, T. Niu, F. Gao, M. W. Khan, Z. Wang, C. Ban, and R. Song, "Distributed secondary control based on bi-limit homogeneity for ac microgrids subjected to non-uniform delays and actuator saturations," *IEEE Transactions on Power Systems*, pp. 1–13, 2024.

[31] Z. Ding, "Distributed time-varying optimization—an output regulation approach," *IEEE Transactions on Cybernetics*, vol. 54, no. 4, pp. 2155–2165, 2024.

[32] S. Sun, J. Xu, and W. Ren, "Distributed continuous-time algorithms for time-varying constrained convex optimization," *IEEE Transactions on Automatic Control*, vol. 68, no. 7, pp. 3931–3946, 2023.

[33] G. Behrendt, M. Longmire, Z. I. Bell, and M. Hale, "Distributed asynchronous discrete-time feedback optimization," *IEEE Transactions on Automatic Control*, vol. 70, no. 6, pp. 3968–3983, 2025.

[34] B. Wang, Q. Fei, and Q. Wu, "Distributed time-varying resource allocation optimization based on finite-time consensus approach," *IEEE Control Systems Letters*, vol. 5, no. 2, pp. 599–604, 2021.

[35] T. Morstyn, B. Hredzak, and V. G. Agelidis, "Network topology independent multi-agent dynamic optimal power flow for microgrids with distributed energy storage systems," *IEEE Transactions on Smart Grid*, vol. 9, no. 4, pp. 3419–3429, 2018.

[36] A. Akhavan, J. C. Vasquez, and J. M. Guerrero, "Stability analysis of parallel grid-forming inverters in asymmetrical conditions," *IEEE Journal of Emerging and Selected Topics in Industrial Electronics*, pp. 1–4, 2023.

[37] E. A. S. Ducoin, Y. Gu, B. Chaudhuri, and T. C. Green, "Analytical design of contributions of grid-forming & grid-following inverters to frequency stability," *IEEE Transactions on Power Systems*, pp. 1–14, 2024.

[38] M. Z. Mansour, M. H. Ravanji, A. Karimi, and B. Bahrani, "Small-signal synchronization stability enhancement of grid-following inverters via a feedback linearization controller," *IEEE Transactions on Power Delivery*, vol. 37, no. 5, pp. 4335–4344, 2022.

[39] A. Bidram, V. Nasirian, A. Davoudi, F. L. Lewis *et al.*, *Cooperative synchronization in distributed microgrid control*. Cham, Switzerland: Springer, 2017.

[40] M. Fazlyab, S. Paternain, V. M. Preciado, and A. Ribeiro, "Prediction-correction interior-point method for time-varying convex optimization," *IEEE Transactions on Automatic Control*, vol. 63, no. 7, pp. 1973–1986, 2018.

[41] A. Iserles, *A First Course in the Numerical Analysis of Differential Equations*, ser. Cambridge Texts in Applied Mathematics. Cambridge: Cambridge University Press, 2009, vol. 44.

[42] T. Xie, G. Chen, and X. Liao, "Event-triggered asynchronous distributed optimization algorithm with heterogeneous time-varying step-sizes," *NEURAL COMPUTING & APPLICATIONS*, vol. 32, no. 10, SI, pp. 6175–6184, MAY 2020.

[43] M. Fazlyab, C. Nowzari, G. J. Pappas, A. Ribeiro, and V. M. Preciado, "Self-triggered time-varying convex optimization," in *2016 IEEE 55TH CONFERENCE ON DECISION AND CONTROL (CDC)*, ser. IEEE Conference on Decision and Control. IEEE; Soc Ind & Appl Math; Inst Operat Res & Management Sci; Japanese Soc Instrument Control Engineers; European Control Assoc, 2016, pp. 3090–3097, 55th IEEE Conference on Decision and Control (CDC), Las Vegas, NV, DEC 12-14, 2016.

[44] S. S. Kia, J. Cortes, and S. Martinez, "Distributed convex optimization via continuous-time coordination algorithms with discrete-time communication," *AUTOMATICA*, vol. 55, pp. 254–264, MAY 2015.

[45] S. Gupta, V. Kekatos, and S. Chatzivasileiadis, "Optimal design of volt/var control rules of inverters using deep learning," *IEEE Transactions on Smart Grid*, pp. 1–1, 2024.

[46] T. Morstyn, B. Hredzak, G. D. Demetriades, and V. G. Agelidis, "Unified distributed control for dc microgrid operating modes," *IEEE Transactions on Power Systems*, vol. 31, no. 1, pp. 802–812, 2016.

[47] R. Zhang, Z. Liu, Z. Bie, and B. Hredzak, "Dynamic clusters supported bi-level control system with lower communication requirements for a distribution network with distributed battery and photovoltaic systems," *IEEE Transactions on Smart Grid*, vol. 15, no. 4, pp. 3824–3838, 2024.

[48] R. Zhang and B. Hredzak, "Distributed control system with aperiodic sampled time-delayed data for batteries and renewable energy sources in microgrid," *IEEE Transactions on Sustainable Energy*, vol. 11, no. 2, pp. 1013–1022, 2020.